



Finite element analyses of rail head cracks: Influence of load characteristics on direction and rate of rolling contact fatigue crack growth

Downloaded from: <https://research.chalmers.se>, 2025-07-01 00:02 UTC

Citation for the original published paper (version of record):

Salahi Nezhad, M., Kabo, E., Ekberg, A. et al (2025). Finite element analyses of rail head cracks: Influence of load characteristics on direction and rate of rolling contact fatigue crack growth. *Engineering Fracture Mechanics*, 325. <http://dx.doi.org/10.1016/j.engfracmech.2025.111322>

N.B. When citing this work, cite the original published paper.



Finite element analyses of rail head cracks: Influence of load characteristics on direction and rate of rolling contact fatigue crack growth

Mohammad Salahi Nezhad ^{a,b},* , Elena Kabo ^c, Anders Ekberg ^{c,d},
Fredrik Larsson ^a

^a Department of Industrial and Materials Science/CHARMEC, Chalmers University of Technology, SE-412 96 Gothenburg, Sweden

^b FS Dynamics Sweden AB, Mölndalsvägen 24, SE-412 63 Gothenburg, Sweden

^c Department of Mechanics and Maritime Sciences/CHARMEC, Chalmers University of Technology, SE-412 96 Gothenburg, Sweden

^d Trafikverket (Swedish Transport Administration), Sweden

ARTICLE INFO

Keywords:

Rolling contact fatigue
Crack propagation
Crack growth rate and direction
XFEM

ABSTRACT

The influence of operational loads on predicted rolling contact fatigue crack growth rates and directions in a rail head is studied. A 3D finite element based numerical framework is adopted featuring a 60E1 rail with an inclined surface-breaking, semi-circular gauge corner crack. The influence of magnitude and position of (normal) contact load, wheel–rail tractive forces, thermal loads, and rail bending under different support conditions is investigated. An accumulative vector crack tip displacement criterion is employed to predict crack growth direction, whereas growth rates are estimated using Paris-type relations. Results are assessed along the crack front for different crack radii. It is found that the crack growth rate is primarily influenced by the contact load magnitude and position. Additional rail bending and thermal loading will somewhat increase predicted growth rates, especially for larger cracks. Crack growth direction under combined loading generally depends on the ratio between the contact load and the bending/thermal load in that poor track support conditions and/or an increased thermal loading (cooling) promote downward growth. Results are useful for rail maintenance planning as illustrated in the study by quantifying the effects of loading conditions on estimated rail life.

1. Introduction

In the wheel–rail interface, contact stresses are on the order of GPa with frictional stresses that can reach hundreds of MPa [1]. Under such conditions Rolling Contact Fatigue (RCF) cracks are essentially unavoidable. The annual maintenance costs of RCF cracks are generally very high [2,3]. However, lack of (or too late) maintenance will increase the required maintenance efforts, and lead to safety risks. A reason is that an RCF crack initially propagates in a fairly shallow angle that progressively becomes deeper. At the depth of some millimetres, the crack may deviate towards a fairly horizontal growth, which leads to limited material fall-out/spalling and requires limited grinding/milling efforts to mitigate. Alternatively, the crack may propagate transversely. This will impose a risk of rail break and requires costly maintenance which may involve rail replacement.

* Corresponding author at: Department of Industrial and Materials Science/CHARMEC, Chalmers University of Technology, SE-412 96 Gothenburg, Sweden.
E-mail address: salahi@chalmers.se (M. Salahi Nezhad).

<https://doi.org/10.1016/j.engfracmech.2025.111322>

Received 8 April 2025; Received in revised form 1 June 2025; Accepted 2 June 2025

Available online 15 June 2025

0013-7944/© 2025 The Authors. Published by Elsevier Ltd. This is an open access article under the CC BY license (<http://creativecommons.org/licenses/by/4.0/>).

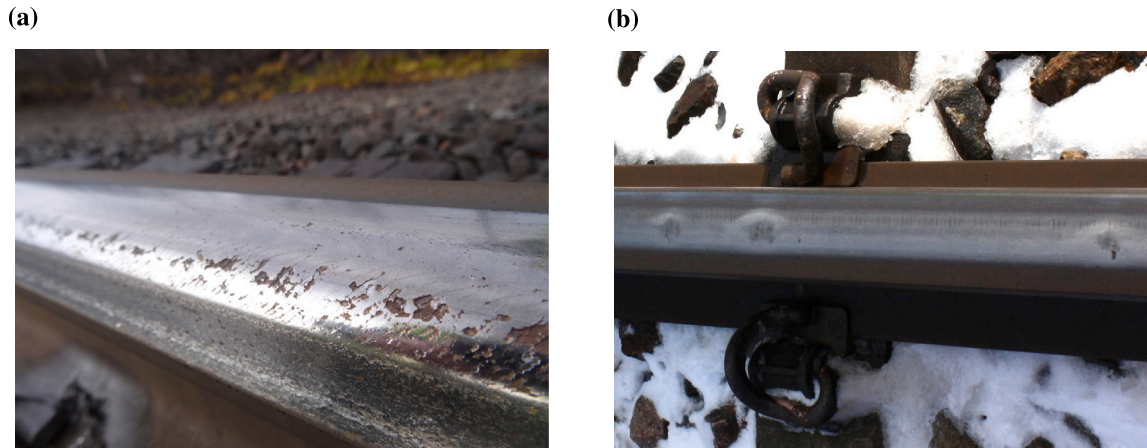


Fig. 1. Two of the most common RCF cracks in railways. (a) Head checks. (b) Squats.

Predicting the conditions under which these scenarios are probable is vital for efficient maintenance planning. The possibility for experimental investigations is limited since the problem does not scale, nor can be reduced to 2D. Consequently, experiments would require full-scale wheel–rail test rigs that, in addition to the contact load, incorporate rail bending and thermal loading.

Numerical simulations are a viable approach for predicting the development of RCF cracks and identifying critical parameters. Several studies have been devoted to predicting Stress Intensity Factors (SIFs) of rail head cracks under wheel–rail loads, see e.g., [4–7]. When it comes to the crack propagation in rails, the majority of the studies mainly investigate crack growth rate as it can be closely related to SIFs, see e.g., [8–10]. However, numerical studies that predict the direction of crack propagation in rails are scarce, and are mainly simplified to 2D. This is because the majority of the criteria to predict growth direction found in the literature fail under rolling contact conditions [11,12]. Examples of such studies are [13–16], where the influence of parameters such as crack inclination, various operational loading scenarios, crack face friction, and tractive forces is investigated in 2D.

With the aim to model the 3D situation at rolling contact fatigue cracks under the influence of varying load parameters, a recently developed numerical framework [17] is adopted. A semi-circular gauge corner crack is modelled using an eXtended Finite Element Method (XFEM). An Accumulative Vector Crack Tip Displacement (AVCTD) criterion is employed to predict crack growth direction. This criterion has previously been validated using 2D simulations for experiments featuring non-proportional mixed-mode loading, and twin disc RCF tests [11,12,15]. Crack growth rates are roughly estimated using Paris-type equations. The studied load cases are wheel–rail frictional contact, combined rail bending and contact, and combined tensile thermal and contact loads.

The numerical approach was previously developed and described in [17]. The novelty of this continued study lies in quantifying the influence of load characteristics. To this end, magnitudes and positions of the contact load and wheel–rail tractive forces are varied. Further, thermal load, and rail bending magnitudes are varied with the latter linked to variations in track stiffness magnitudes.

Results of the study should be valuable in maintenance planning by quantifying the relative influence of different load scenarios. This is illustrated by an example in Section 3.4 that also serves as a validation that predicted fatigue lives are of a correct order of magnitude. Finally, the study provides an insight into what differentiates squat-type rail cracks (see Fig. 1) from studs [18], which has an impact on how to mitigate these defects.

2. Modelling approach

The modelling framework is presented in detail in [17]. Here, only a brief summary is provided.

2.1. Crack propagation

Crack growth rate and direction for a stationary crack are predicted from Stress Intensity Factors (SIFs) computed using a displacement-based method described in [19].

2.1.1. Direction of crack growth

RCF crack may experience stable shear growth, a transition from shear to tensile growth, and/or tensile growth, depending on the crack size and loading. Investigations show that predictions of an Accumulative Vector Crack Tip Displacement (AVCTD) criterion fit experimental results better than other investigated criteria under all three growth modes considering proportional and non-proportional mixed-mode loading under 2D conditions [11]. Additionally, the AVCTD criterion performs well in simulating twin disc experiments [12,15] and predicts crack growth directions aligning with field observations [20]. Hence, the AVCTD criterion proposed in [11] and modified in [15] is employed. Since the criterion only accounts for mode I and II loading, and due to the

absence of (substantial) experimental data in the literature to advise differently, this study disregards any potential influence of mode III on crack growth direction (but not on rate).

In the AVCTD criterion, crack face opening displacement, $\delta_I(t)$, and crack face sliding displacement, $\delta_{II}(t)$, at time instance t are evaluated from SIFs ($K_I(t)$ and $K_{II}(t)$), which reflect the overall loading of the crack. Choosing evaluation points for δ_I and δ_{II} is more complex than in 2D where the crack front is represented by a point. Following [21], the displacement fields in the vicinity of a point on the crack front are evaluated presuming plane strain conditions. The crack face displacements are computed as the difference between the top and bottom surface crack face displacements ($\vartheta = \pi$, and $\vartheta = -\pi$, respectively in the crack local coordinate system shown in Fig. 2c). Opening, $\delta_I(d, t)$, and sliding, $\delta_{II}(d, t)$, displacements at a radial distance d from the studied point on the crack front are then evaluated as

$$\begin{aligned} \delta_I(d, t) &= u_{\perp}(d, \pi, t) - u_{\perp}(d, -\pi, t) = B(d)K_I(t), \\ \delta_{II}(d, t) &= u_{\parallel}(d, \pi, t) - u_{\parallel}(d, -\pi, t) = B(d)K_{II}(t). \end{aligned} \quad (1)$$

Here, $B(d) = \frac{8(1-\nu^2)}{E} \sqrt{\frac{d}{2\pi}}$, where $\nu = 0.3$ is Poisson's ratio and $E = 210$ GPa is elastic modulus of the rail steel. In this study, $d = 1$ mm is employed, and minor crack face penetrations in numerical simulations are eliminated by truncating (minute) negative values of $K_I(t)$. The 'amplitudes' of $\delta_I(t)$ and $\delta_{II}(t)$ are determined using mid-values over the load cycle, $\bar{\delta}_{I/II} = \frac{1}{2} \left[\max_t (\delta_{I/II}(t)) + \min_t (\delta_{I/II}(t)) \right]$, as

$$\bar{\delta}_{I/II}(t) = \delta_{I/II}(t) - \bar{\delta}_{I/II}. \quad (2)$$

The instantaneous crack growth direction $\vartheta(t)$, shown in Fig. 2c, and instantaneous crack driving displacement $\delta_a(t)$ are evaluated as

$$\vartheta(t) = \arcsin \left(\frac{-\bar{\delta}_{II}(t)}{\delta_a(t)} \right), \quad (3)$$

and

$$\delta_a(t) = \sqrt{\langle \bar{\delta}_I(t) \rangle^2 + 2\langle \bar{\delta}_I(t) \rangle |\bar{\delta}_{II}(t)| + 2\bar{\delta}_{II}(t)^2}. \quad (4)$$

Here, $\langle \bullet \rangle := \frac{1}{2} (\bullet + |\bullet|)$ are Macaulay brackets.

The crack driving displacement vector, Δc , is computed considering the 'rate-independent' response over the load cycle

$$\Delta c = \int_0^{T_c} \left\langle \frac{d\delta_a(t)}{dt} \right\rangle \hat{e}_{\vartheta}(t) dt, \quad (5)$$

where, T_c is the duration of the load cycle. Additionally, \hat{e}_{ϑ} denotes the unit vector in the direction of the instantaneous crack growth direction, $\vartheta(t)$, determined from Eq. (3).

The accumulated crack propagation direction for the entire load cycle, ϕ , in the local coordinate system of the crack (Fig. 2c) is defined by the unit vector

$$\hat{e}_{\phi} = \frac{\Delta c}{\|\Delta c\|}. \quad (6)$$

2.1.2. Rate of crack growth

The crack growth rate (da/dN) can, according to Paris law [22], be predicted as $da/dN = C(\Delta K)^m$. Here, C and m are material parameters. Two Paris-type equations are employed in this study for rate predictions to account for various mode interactions, see [23] for modes I and II. The loading is first assumed to be sequential without any mode overlap. This will result in a lower estimate for the growth rate, computed as

$$\left(\frac{da}{dN} \right)_{lo} = C(\Delta K_I)^m + C(\Delta K_{II})^m + C \left(\frac{\Delta K_{III}}{\sqrt{1-\nu}} \right)^m. \quad (7)$$

Here, $\nu = 0.3$ is Poisson's ratio. Further, $C = 2.47 \times 10^{-9} \frac{\text{mm/cycle}}{(\text{MPa}\sqrt{\text{m}})^m}$ and $m = 3.33$ (for rail steel UIC900 A [24]) are taken the same for all three modes¹.

Alternatively, the loading from different modes can be considered to act simultaneously, providing an upper estimate for the crack growth rate

$$\left(\frac{da}{dN} \right)_{up} = C(\Delta K_{eq})^m. \quad (8)$$

Here, ΔK_{eq} is derived from the energy release rate under plane strain conditions, see [25],

$$\Delta K_{eq} = \sqrt{\Delta K_I^2 + \Delta K_{II}^2 + \frac{1}{1-\nu} \Delta K_{III}^2}. \quad (9)$$

As a result of having non-negative SIF ranges for all three modes ($\Delta K = \max_t (K(t)) - \min_t (K(t))$), the choice of incorporating ΔK_{III} in the lower estimate of crack growth rate (Eq. (7)) results in the explicit inequality $\left(\frac{da}{dN} \right)_{up} \geq \left(\frac{da}{dN} \right)_{lo}$.

¹ The authors are aware that this assumption introduces inaccuracies in absolute quantitative rate predictions, but believe it to be sufficient for the current comparisons of load scenarios.

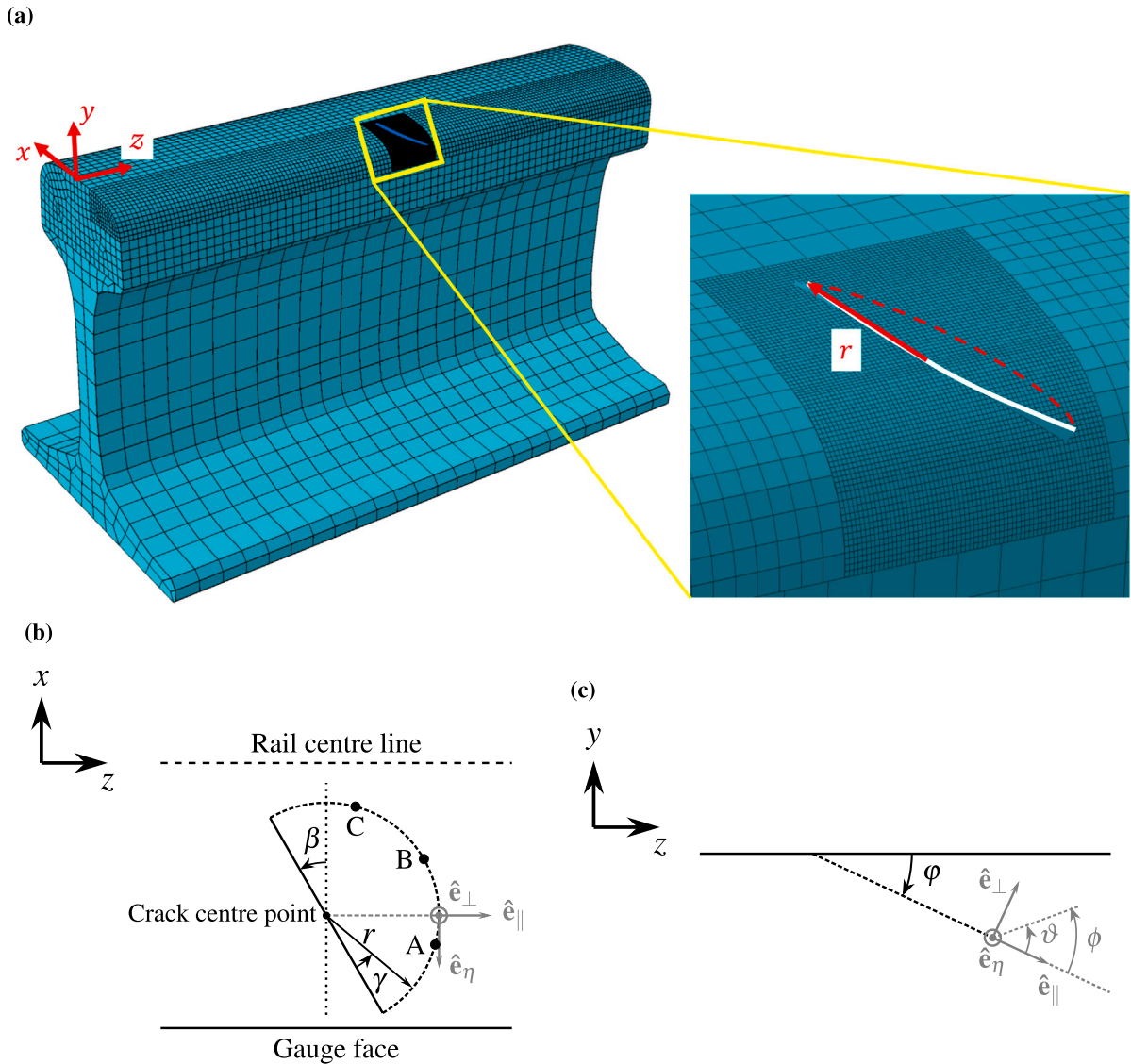


Fig. 2. (a) Employed FE mesh for the 3D model of a cracked rail including a zoomed-in view. The element size in the crack area is 0.4 mm. The global Cartesian coordinate system (x, y, z) is shown. Crack plane inclination characterised by angles φ and β in (b) and (c) where the local coordinate system $(\hat{e}_\parallel, \hat{e}_\perp, \hat{e}_r)$ for a point on the crack front is shown. (b) Top view of the xz -plane: point A is positioned on the gauge side where $\gamma = 45^\circ$, B is at the centre of the crack front with $\gamma = 90^\circ$, and C is located on the field side where $\gamma = 135^\circ$. (c) Side view of the yz -plane. Instantaneous crack growth direction, $\vartheta(t)$, and accumulated crack propagation direction for the entire load cycle, ϕ , are shown.

2.2. Finite element model

Fig. 2a shows the FE model of 300 mm long, and 172 mm high 60E1 rail profile [26]. An isotropic linear elastic material is presumed, with an elastic modulus of $E = 210$ GPa and a Poisson's ratio of $\nu = 0.3$. Standard first-order hexahedral (8-noded brick) elements [27] are employed for discretising the 3D FE model. The bottom surface of the FE model is constrained in the lateral (global x -) and vertical (global y -) directions under all studied cases. Boundary conditions on the vertical surfaces of the rail sides differ based on the applied loads, as described in Section 2.3.

An inclined (quasi) semi-circular crack with a radius, r , is modelled. Following field observations of head checks [28], the surface-breaking crack is positioned at the gauge corner of the rail head, with the crack centre along the rail surface at $(x, z) = (-26.0, 150.0)$ mm as shown in Fig. 2. Also, motivated by field observations [28–30], the inclination for the crack plane is set as $\varphi = 25^\circ$ and $\beta = 27^\circ$, see Figs. 2b and 2c. Simulations are carried out for four crack radii ($r = 3, 5, 9, 13$ mm).

The FE model was implemented in ABAQUS/CAE [31]. The crack is stationary and modelled using XFEM [32,33], whereby the discontinuity in displacements along the crack is modelled explicitly, without affecting the underlying discretisation. This feature

eliminates the need to align the FE mesh with the crack geometry, which would be required in conventional FE analyses. It also removes comparative discretisation errors between different crack sizes as the same FE mesh can be employed in all analyses. A penalty formulation is employed to enforce crack closure constraints, assuming frictionless crack faces. The latter is considered assuming the crack faces are well lubricated at the gauge corner. Lubricants can also pressurise the crack faces due to penetrated fluid. However, it has been shown in field tests [34] that the crack (or parts of it) needs to be fully sealed for pressurisation to happen. As rail crackings in reality are more related to a network of cracks [35], this can rarely happen and the pressurisation effect is thus neglected in this study.

2.3. Loads

Considered loads are wheel–rail contact loads (normal and longitudinal), rail bending, and loading resulting from restricted thermal contraction.

2.3.1. Contact load

The wheel–rail contact is considered by employing a Hertzian semi-ellipsoid pressure distribution over an elliptical contact patch with semi-axes a in the lateral x -direction and b in the longitudinal z -direction, see Fig. 3a. The contact pressure distribution for a wheel load position, (\bar{x}, \bar{z}) , is then [36]

$$p_y(\bar{x}, \bar{z}; x, z) = \begin{cases} \frac{3P}{2\pi ab} \sqrt{1 - \left(\frac{x-\bar{x}}{a}\right)^2 - \left(\frac{z-\bar{z}}{b}\right)^2} & \text{for } \left(\frac{x-\bar{x}}{a}\right)^2 + \left(\frac{z-\bar{z}}{b}\right)^2 \leq 1 \\ 0 & \text{for } \left(\frac{x-\bar{x}}{a}\right)^2 + \left(\frac{z-\bar{z}}{b}\right)^2 > 1 \end{cases}, \quad (10)$$

where P is the vertical wheel load. The semi-axes of the contact patch are determined for contact between a wheel with a rolling radius of 0.46 m and a rail with a transverse head radius of 0.3 m with the same elastic material properties [37]. Here, a larger radius than the gauge corner radius of a nominal rail profile (0.08 m) is employed to account for the occurrence of the rail head radius increase due to wear-in under operational conditions and required grinding.

The Hertzian contact pressure is numerically imposed as vertical traction on the curved rail surface. Full slip conditions featuring a traction coefficient f_{wr} are assumed to evaluate wheel–rail tractive stresses in the z -direction as $p_t(\bar{x}, \bar{z}; x, z) = f_{wr} p_y(\bar{x}, \bar{z}; x, z)$. In the lateral x -direction, no tractive stresses are considered in this study, corresponding to a wheelset negotiating a curve with radial steering at balanced speed.

The current study investigates head checks [38], which are predominantly observed in curved sections with wheel–rail contact at the gauge shoulder of the rail [28]. A sequence of multi-body simulations of wagons negotiating a 1500 m curve conducted with a spectrum of measured wheel profiles concluded that the wheel–rail contact occurred with an offset of some 15–25 mm from the top of the rail [39]. Motivated by this, the contact load is initially applied with an offset of $\bar{x} = -19$ mm (see Fig. 3) in the global coordinate system of Fig. 2a.

Hertzian theory assumes uniform curvatures within the contact zone. This is compromised at the gauge shoulder [40]. To bypass this issue², it is presumed in the Hertzian analyses that the wheel–rail contact takes place at a plane with a constant inclination tangent to the rail surface at the theoretical contact point, see Fig. 3b. Normal, p_n , and tangential, p_ξ , stress components are consequently evaluated from the projection of the vertical contact pressure, p_y in Eq. (10), on this plane. Also, all three stress components (p_n , p_ξ , p_t) have the same spatial elliptical distribution as given in Eq. (10), but different peak magnitudes.

In the FE analyses, the contact stress distribution is applied as a moving contact load with three components (p_n , p_ξ , p_t), see Fig. 3b. The load traverses the rail section in the positive z -direction to simulate a wheel passage. Longitudinal tractive stresses, p_t , act in the negative z -direction, leading to the opening of the rail crack as the load moves towards the crack mouth, which will facilitate crack face sliding (and, in operations, penetration of water) [41]. Note that wheel–rail traction (e.g., caused by dry/wet conditions) is characterised through a varying traction coefficient f_{wr} , whereas crack face contact in this study is presumed frictionless. In practice, the situation is more complex as dry conditions would gradually dry out crack face lubricants. In addition, wear debris that forms in the crack will alter friction, and may introduce wedge effects [42].

Under pure contact load, the vertical rail sides in the numerical model are constrained in the longitudinal direction ($u_z^p = 0$).

2.3.2. Rail bending

A passing wheel imposes bending of a rail. To quantify the vertical deflection and resulting longitudinal rail stresses, the in-house code DIFF [43] was employed for analysis of the vertical dynamic vehicle–track interaction at different wheel loads and track support conditions.

In the simulations, a perfectly round wheel traverses a track section with nominal geometry at 100 km/h. Symmetry is employed and the ballast stiffness for a half-sleeper is taken as 50 MN/m (‘nominal’ support conditions) or 20 MN/m (‘poor’ support conditions). The sleeper spacing is 0.6 m and the remaining track parameters follow [14]. Investigated wheel load magnitudes are 7.5 t and 11.25 t.

² Alternatively, a more sophisticated contact model can be used. However, this makes the results of the parametric study significantly more complex to interpret.

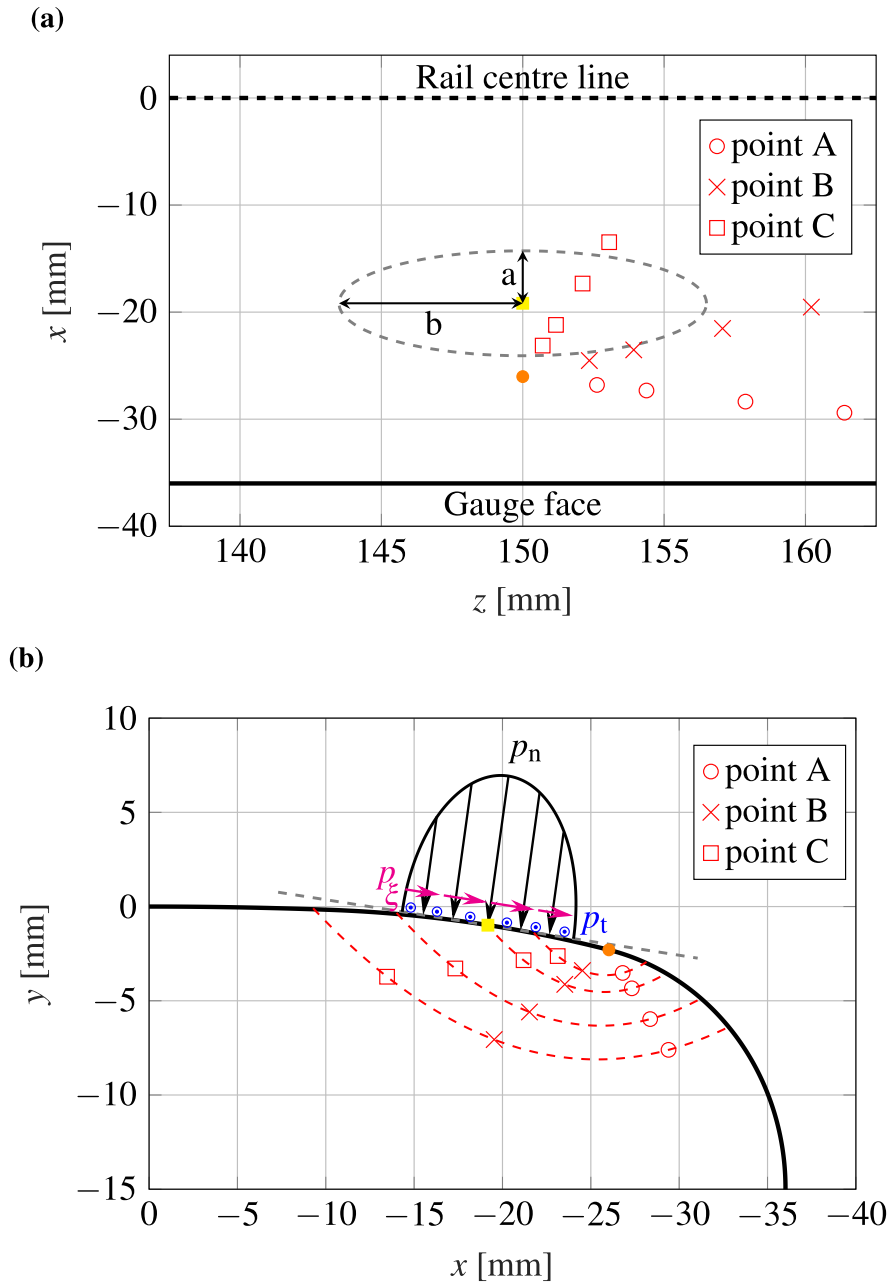


Fig. 3. Points (A, B and C) on the crack front where analyses are performed. Centre of contact load indicated by a yellow square, while centre point of the crack (for all radii) is marked with a solid orange circle. (a) Top view (xz - plane) where dashed curve indicates contact patch. (b) Side view (xy - plane) where the grey dashed line indicates the plane tangent to the rail profile at the centre of the contact load.

The variation of the bending moment at a position above a sleeper, which is the most detrimental position for a head check, is shown in Fig. 4 as a function of the wheel load position, \bar{z} . Here, $\bar{z} = 0.15$ m represents a wheel load longitudinally positioned at the centre of the crack mouth.

The bending moment load is applied as longitudinal boundary displacements on the vertical rail sides, see Fig. 2a. Displacements are computed using moment–curvature relation for an Euler–Bernoulli beam, following [14], as

$$u_z^p(\bar{z}; x, y, \frac{L}{2} \pm \frac{L}{2}) = \frac{\pm M(\bar{z}) [h_c + y] L}{2E I_x}, \tag{11}$$

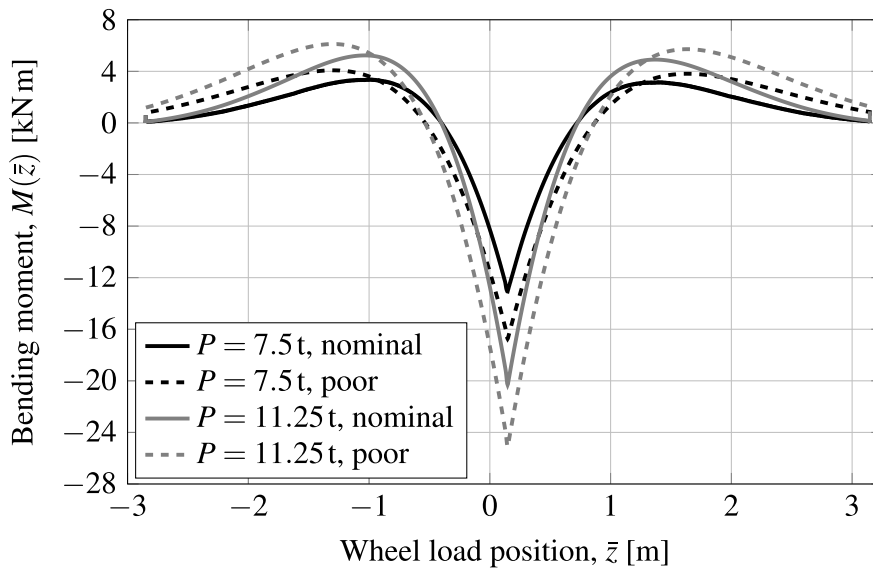


Fig. 4. Bending moment at the position of the crack mouth centre as a function of the longitudinal position of the wheel, \bar{z} , for different wheel loads, P , and track support conditions ('nominal' or 'poor'). Results derived from DIFF simulations [43].

where $u_z^p(\bar{z}; x, y, z)$ represents the prescribed displacements at coordinates (x, y, z) for a given load position \bar{z} . $M(\bar{z})$ denotes the bending moment, and L the length of the modelled rail section. Further, $h_c = 0.091$ m is the vertical distance from the top surface of the rail to the neutral axis, and $I_x = 30.5 \times 10^{-6} \text{ m}^4$ is the moment of inertia for the considered rail profile, see [26].

2.3.3. Thermal loading

In continuously welded rails, a temperature deviation from the stress-free rail temperature, T_0 , causes longitudinal stresses as a result of the restricted contraction. These are here evaluated using a linear thermoelasticity assumption, and imposed as equivalent boundary displacements on the vertical rail sides [14]

$$u_z^p(x, y, \frac{L}{2} \pm \frac{L}{2}) = \mp \alpha \Delta T \frac{L}{2}. \quad (12)$$

Here, $u_z^p(x, y, z)$ denotes the prescribed displacements at the coordinates (x, y, z) , $\alpha = 11.5 \times 10^{-6} [1/^\circ\text{C}]$ is the thermal expansion coefficient of the rail material, and L is the length of the considered rail section. Further, $\Delta T = T - T_0$, where T is the rail temperature.

2.4. Numerical implementation

Post-processing of results from FE analyses, as outlined in Section 2.1, was conducted using MATLAB [44]. Predicted growth directions and rates were assessed at three distinct points along the crack front, see Fig. 2b. In the following sections, predicted crack growth directions are shown in the local coordinate system of the crack in terms of ϕ (see Fig. 2c), where $\phi = 0$ represents the initial slope of the crack, $\phi > 0$ indicates a tendency for upward kinking, and $\phi < 0$ indicates a tendency for growth downward from the current crack plane.

3. Influence of variations in operational loads

3.1. Influence of wheel–rail contact loads

In this study, a vertical wheel load, $P = 7.5 \text{ t}$ is considered as the reference case³. Semi-axes of the contact patch become $a = 4.9$ mm and $b = 6.5$ mm. Peak contact stress components for $f_{\text{wr}} = 0$ and $f_{\text{wr}} = 0.3$ become $(p_n, p_\xi, p_t) = (1091, 161, 0)$ MPa, and $(p_n, p_\xi, p_t) = (1091, 161, 331)$ MPa, respectively, see Fig. 3b. A wheel load of $P = 11.25 \text{ t}$ corresponds to $a = 5.6$ mm and $b = 7.4$ mm, and $(p_n, p_\xi, p_t) = (1258, 185, 0)$ MPa and $(p_n, p_\xi, p_t) = (1258, 185, 381)$ MPa for $f_{\text{wr}} = 0$ and $f_{\text{wr}} = 0.3$, respectively.

Fig. 5 presents predicted directions of crack growth. For $P = 7.5 \text{ t}$ and $f_{\text{wr}} = 0$ the crack tends to kink upwards in the reference case for all investigated points and crack sizes with the exceptions of points B and C at $r = 9$ mm. This discrepancy is likely due to the occurrence of the severe crack closure as these points are located (nearly) under the peak contact pressure, see Fig. 3b.

³ $P = 7.5 \text{ t}$ implies a wheel load of $P = 7500 \text{ g} = 73575 \text{ N}$, where g denotes the gravitational acceleration.

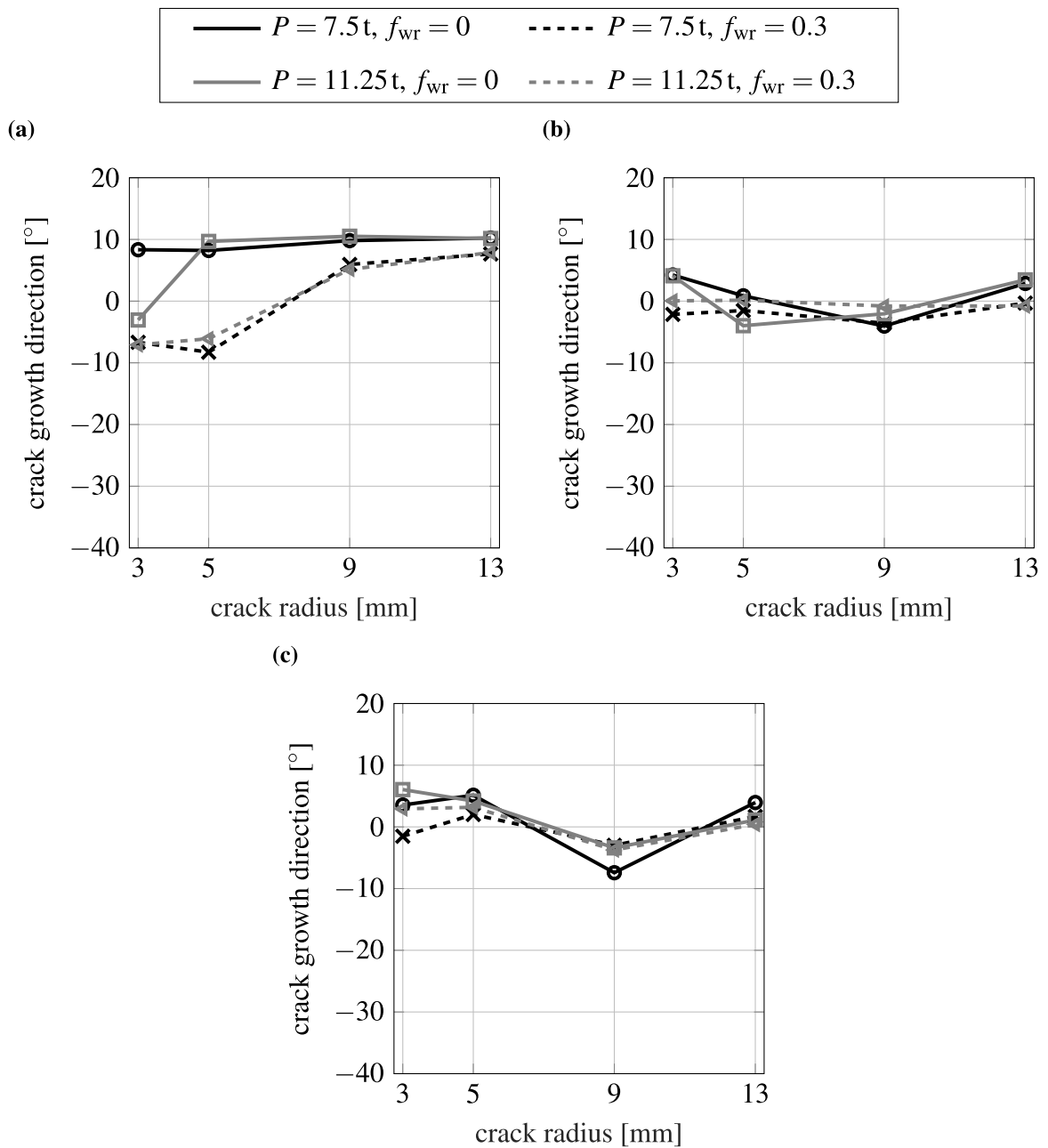


Fig. 5. Predicted local crack growth directions ϕ under contact load for different crack radii r . Evaluations at points (a) A, (b) B, and (c) C, see Figs. 2b, 2c, and 3.

The upward kinking trend is also generally seen for the $P = 11.25t$ case. Deviation is observed for point B when $r = 5$ mm or $r = 9$ mm, and for point C for $r = 9$ mm. Also here the likely cause is severe crack closure. Further, the higher load promote downward crack growth at point A for a $r = 3$ mm crack.

As shown in Fig. 5, adding tractive stress with $f_{wr} = 0.3$ generally promotes more downward crack growth in the reference case since the considered tractive stress opens up the crack as it approaches the mouth. For points experiencing severe crack closure, the tractive stress provides release, leading to a shallower growth direction. This behaviour is also seen for $P = 11.25t$.

Predicted growth rates are shown in Fig. 6 (only upper estimates given here as lower estimates have similar magnitudes). In general, the crack growth rate increases with increasing crack radius. Further, the addition of a tractive stress p_t increases crack growth rate for smaller cracks, $r \leq 5$ mm. For larger cracks, the tractive stress instead has an arresting effect. For the $r = 13$ mm

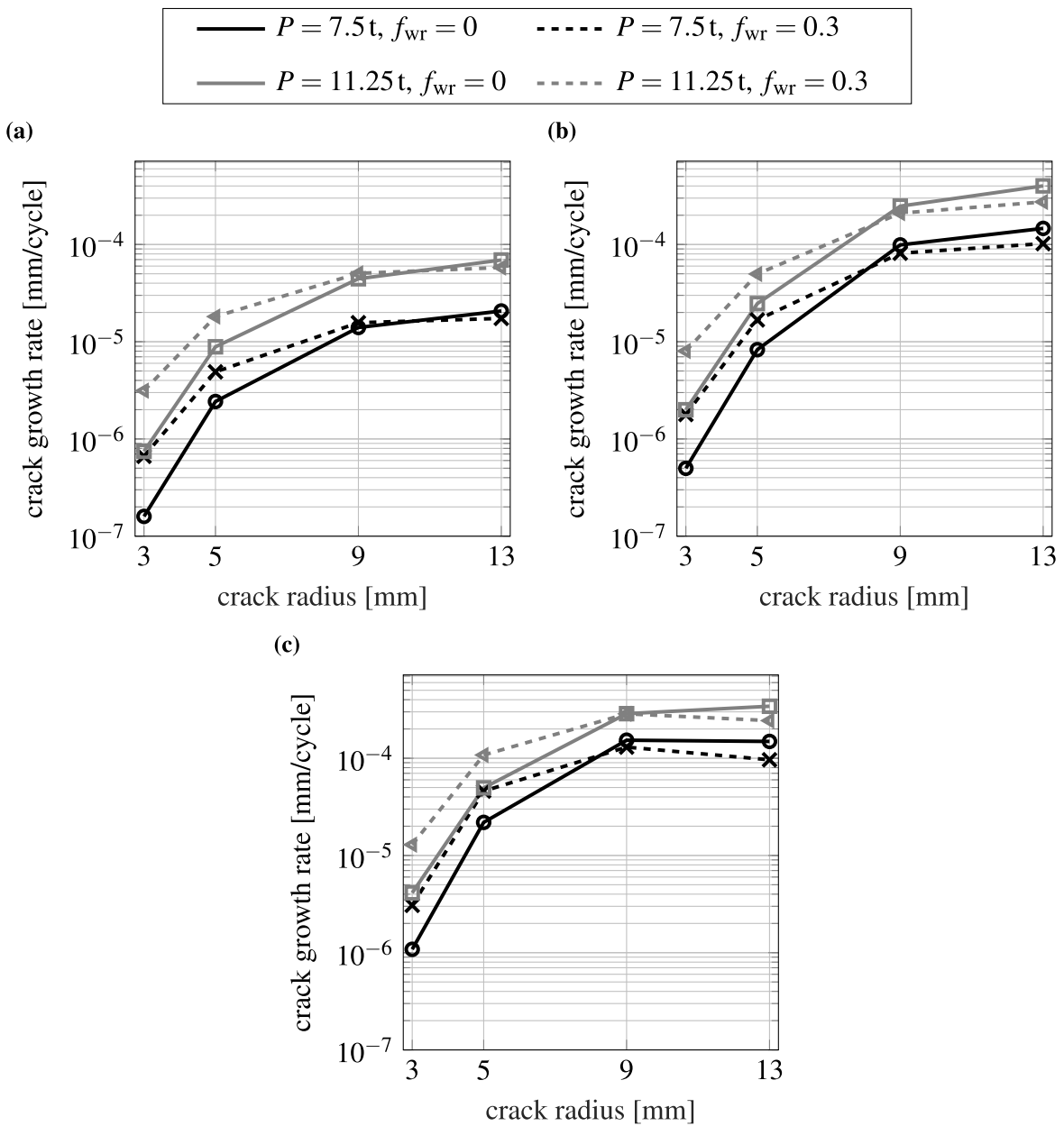


Fig. 6. Upper estimates of predicted crack growth rates under contact load for different crack radii r . Evaluation at points (a) A, (b) B, and (c) C, see Figs. 2b, 2c, and 3.

crack this effect is so large, especially at point C, that growth rate is reduced by crack size, see Fig. 6. Results for $P = 11.25t$ follow the same trend and feature higher growth rates.

Lastly, the influence of the contact load position is studied for a contact load of $P = 7.5t$ and $f_{wr} = 0$. To this end, the centre of the contact load is shifted laterally 2 mm closer to the gauge side, i.e., from $\bar{x} = -19\text{ mm}$ to $\bar{x} = -21\text{ mm}$. Fig. 7 shows predicted growth directions. For $f_{wr} = 0$ results for $\bar{x} = -21\text{ mm}$ generally predict similar growth directions as for $\bar{x} = -19\text{ mm}$. Deviations are seen at point B for $r \leq 9\text{ mm}$ and at point C for $r = 9\text{ mm}$. The reason is that the shift to $\bar{x} = -21\text{ mm}$ causes severe crack closure for point B to shift towards smaller crack sizes, $r \leq 5\text{ mm}$. Further, point C for $r = 9\text{ mm}$ becomes less affected by crack closure due to the increased distance to the contact load. Adding tractive stress generally increases the propensity for more downward crack growth also for the $\bar{x} = -21\text{ mm}$ case.

Crack growth rates for the $\bar{x} = -21\text{ mm}$ case show similar trends as for $\bar{x} = -19\text{ mm}$ but with generally higher growth rates, see Fig. 8. The drop in growth rate for point C from $r = 9\text{ mm}$ to $r = 13\text{ mm}$ is more pronounced for the $\bar{x} = -21\text{ mm}$ case, which can

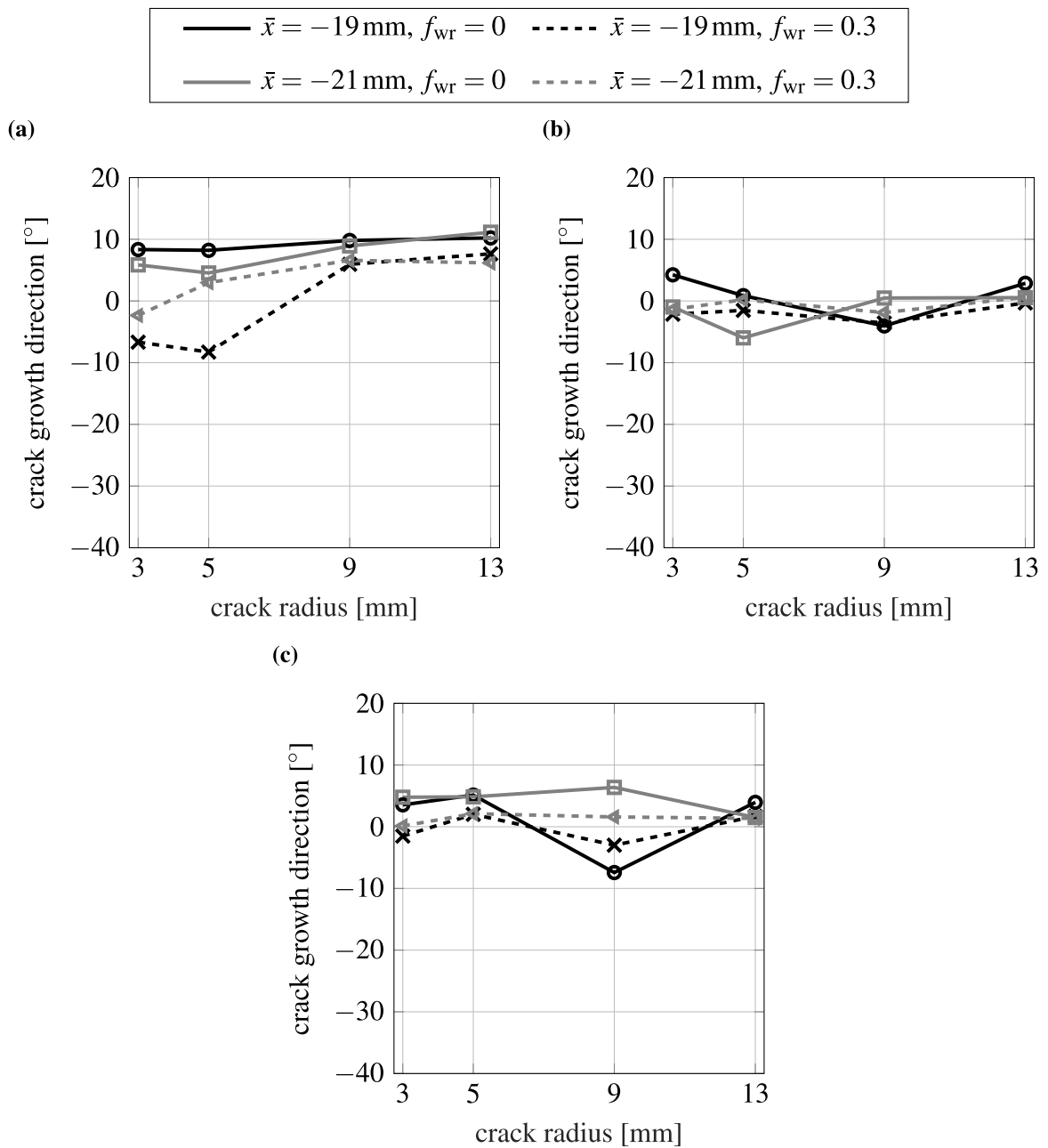


Fig. 7. Predicted crack growth directions under contact load of $P = 7.5 \text{ t}$ centred at $\bar{x} = -19 \text{ mm}$ and $\bar{x} = -21 \text{ mm}$ for different crack radii, evaluated at points (a) A, (b) B, and (c) C.

be expected due to the increased distance to the load. It is noted that shifting the contact load towards the gauge side reduces the difference in predicted growth rates between point A and points B and C.

3.2. Influence of rail bending

Rail bending corresponding to ‘nominal’ (half-sleeper ballast stiffness of 50 MN/m) and ‘poor’ (20 MN/m) track support conditions, see Section 2.3.2, are considered in combination with contact load. A load of $P = 7.5 \text{ t}$, $f_{wr} = 0.3$ and bending under ‘nominal’ track support conditions is considered as the reference case.

As shown in Fig. 9, cracks subjected to combined bending and contact load typically tend to grow deeper into the rail head due to the additional tensile loading at the beginning and the end of the load cycle, see Fig. 4. The effect is most pronounced in point

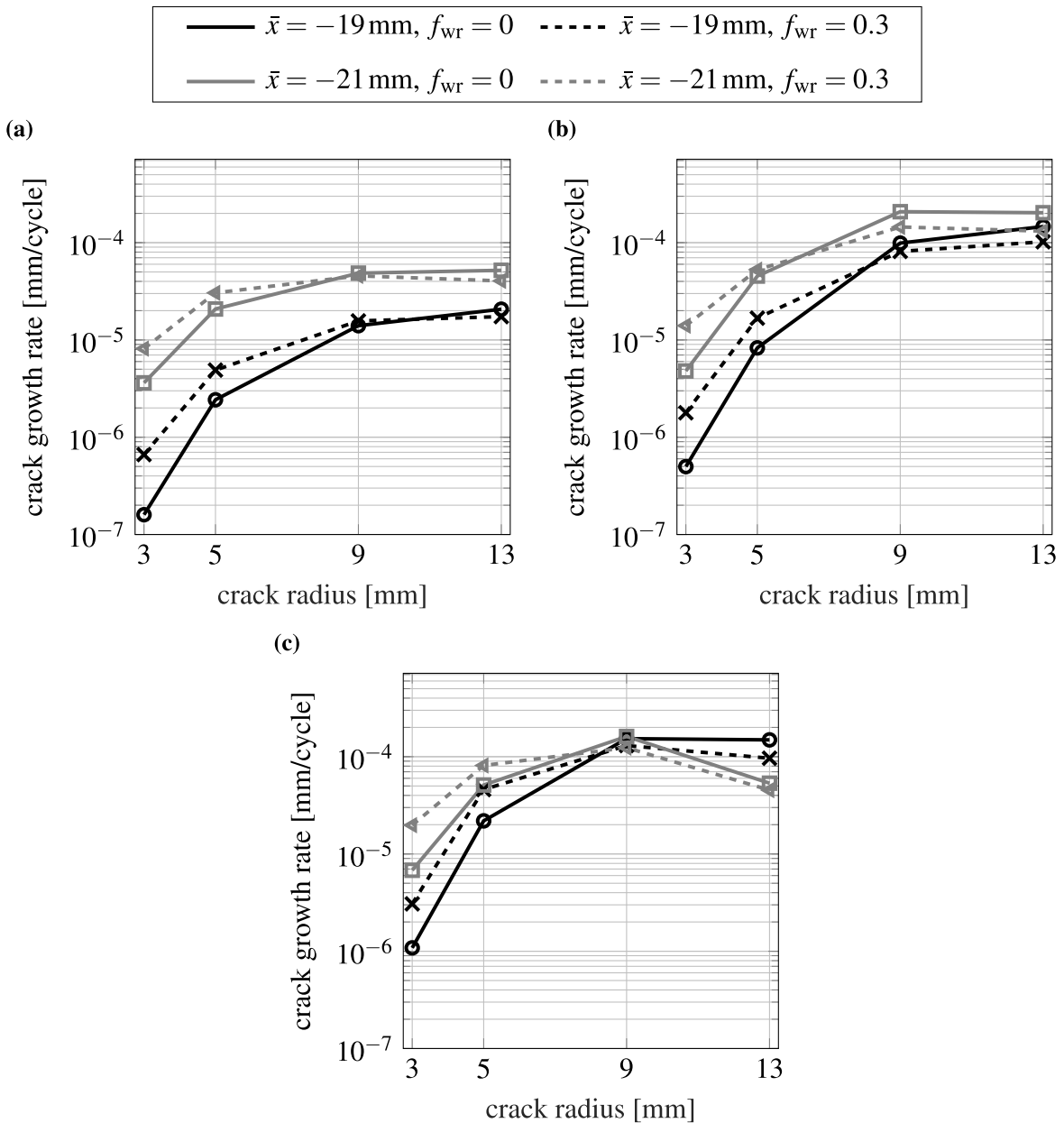


Fig. 8. Upper estimates of predicted crack growth rates under contact load of $P = 7.5$ t centred at $\bar{x} = -19$ mm and $\bar{x} = -21$ mm for different crack radii, evaluated at points (a) A, (b) B, and (c) C.

A (at the gauge side) and least pronounced in point C (at the centre side), and aggravated by ‘poor’ track support conditions. The trends are the same for an increased wheel load ($P = 11.25$ t).

Predicted crack growth rates under combined bending and contact load are presented in Fig. 10. In general, adding a bending slightly increases growth rates with a somewhat more pronounced effect under ‘poor’ track support conditions. Lower (not shown here) and upper estimates follow the same trends with similar magnitudes.

Predicted directions of crack growth for a contact load position of $\bar{x} = -21$ mm are given in Fig. 11. These show a general tendency for shallower propagation. This can be expected as the movement of the contact load towards the gauge side (i.e., closer to the crack) increases the influence of the contact load in relation to the bending load. In particular this is the case for point A. This is also the reason for the generally higher crack growth rates in the $\bar{x} = -21$ mm case, see Fig. 12. In particular, the marked rate increase for point A makes the crack growth rates more similar along the crack front. For larger cracks, the increased distance between the contact load and point C causes growth rates to decrease here.

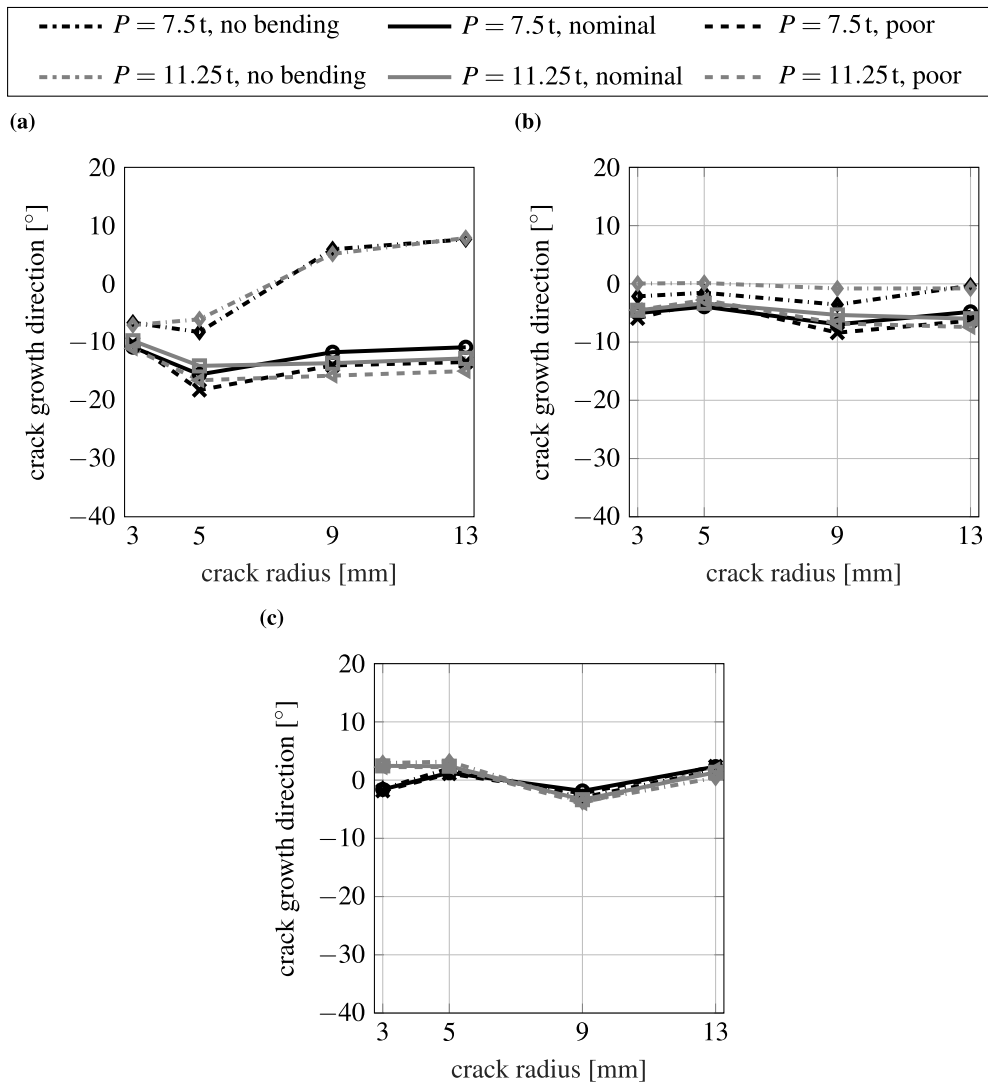


Fig. 9. Predicted crack growth directions under combined bending and wheel load P with $f_{wr} = 0.3$ for different crack radii, evaluated at points (a) A, (b) B, and (c) C.

3.3. Influence of temperature

The influence of low temperatures during wheel passage simulations is considered. For the thermal part of the load, $\Delta T = 0^\circ\text{C}$ (pure contact load), $\Delta T = -20^\circ\text{C}$ and $\Delta T = -30^\circ\text{C}$ are considered and applied as boundary displacements following Eq. (12). In the following, the combined load of $P = 7.5$ t, $f_{wr} = 0.3$ and $\Delta T = -20^\circ\text{C}$ is considered as the reference case. As motivated in [15], mid-values of crack face displacements over a load cycle, cf. Eq. (2), are evaluated only considering the contact load for this combined load. In short, this is because the numerous contact load cycles within a single thermal cycle will shakedown the contact stress response, but not the thermal response.

Predicted directions of crack growth given in Fig. 13 show that cold temperatures generally promote deeper crack growth due to the imposed tension. An increase in the thermal load magnitude ($P = 7.5$ t, $f_{wr} = 0.3$ and $\Delta T = -30^\circ\text{C}$) promotes even more downward growth, as expected. A higher wheel load ($P = 11.25$ t, $f_{wr} = 0.3$ and $\Delta T = -20^\circ\text{C}$) leads to shallower crack growth as compared to the reference case. The combination of $P = 11.25$ t, $f_{wr} = 0.3$ and $\Delta T = -30^\circ\text{C}$ gives predicted crack growth directions very close to the reference case as the effects of increased contact and thermal loads are cancelling each other.

Crack growth rate predictions are shown in Fig. 14. The reference case generally has slightly higher growth rates than for pure contact. Lower temperatures and higher wheel loads generally increase crack growth rates. Lower and upper estimates follow the same trend with similar magnitudes.

The influence of contact load position is also studied for the reference case. Fig. 15 shows that predicted directions generally become shallower (closer to $\phi = 0^\circ$) for the $\bar{x} = -21$ mm case. Similar to the effect discussed in Section 3.2, a contact load applied

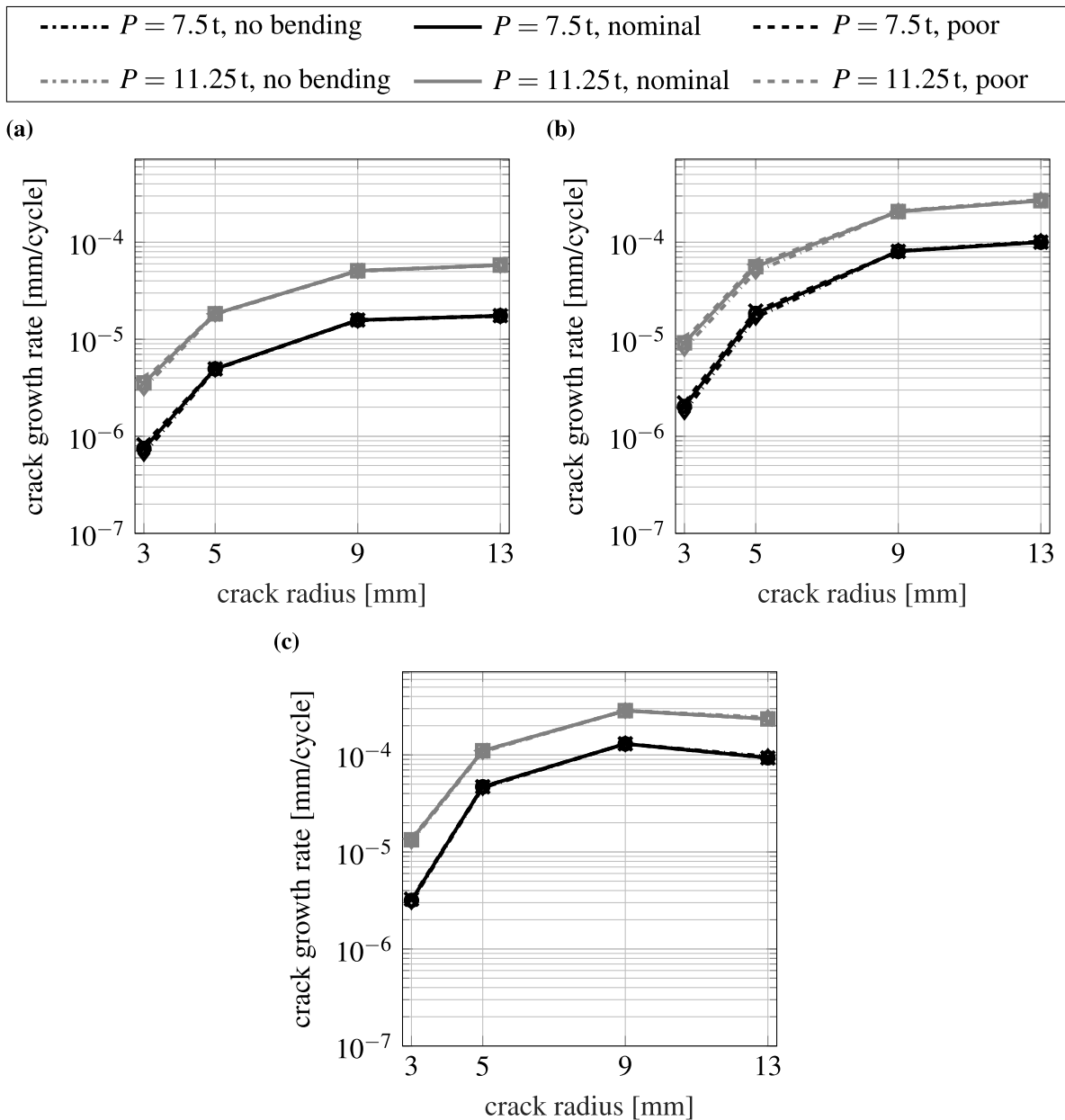


Fig. 10. Upper estimates of predicted crack growth rates under combined bending and wheel load P with $f_{wr} = 0.3$ for different crack radii, evaluated at points (a) A, (b) B, and (c) C.

closer to the gauge side generally emphasises the effect of the contact load in relation to the thermal load, especially for point A. As also discussed in Section 3.2, a contact load position closer to the gauge side results in increased crack growth rates, see Fig. 16. The exception is point C where growth rates decrease for larger cracks ($r \geq 9$ mm) in the $\bar{x} = -21$ mm case.

3.4. Fatigue life estimation

Evaluation of remaining fatigue life is a way to support maintenance planning. This can be done by integrating predicted crack growth rates assuming linear variation of growth rate between two consecutive data points. The amount of passing traffic can then be evaluated by multiplying the fatigue life by the axle load. Fig. 17a shows the passing traffic in Mega Gross Tonnes (MGT) for the reference case under combined bending and contact load taking the smallest crack, $r = 3$ mm, to be the initial crack. From the varying growth rate estimates along the crack front, considering one point at a time (A, B and C), it is seen that the rail life reduces

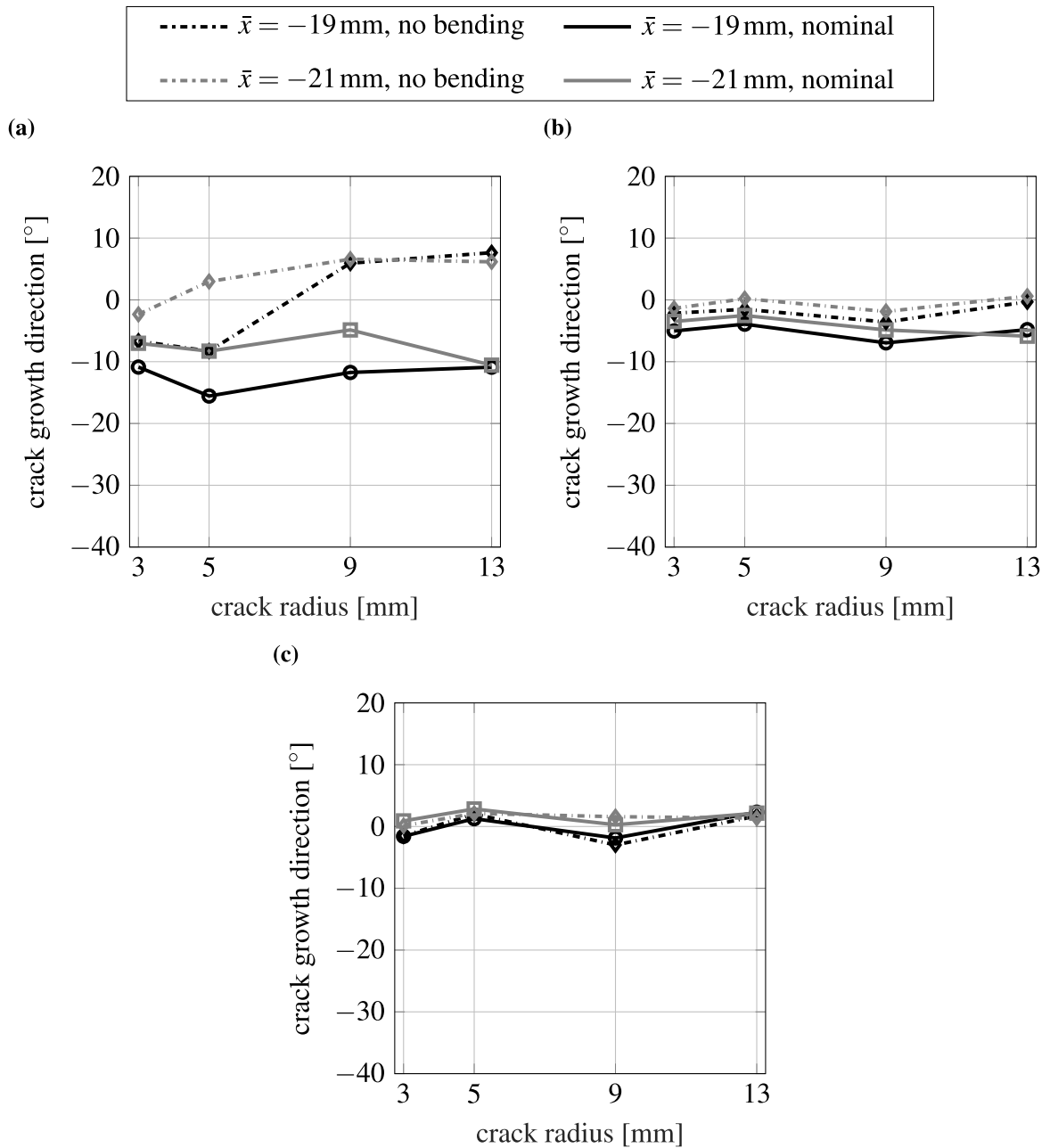


Fig. 11. Predicted crack growth directions under combined bending with ‘nominal’ track support conditions and a wheel load of $P = 7.5$ t with $f_{wr} = 0.3$ centred at $\bar{x} = -19$ mm and $\bar{x} = -21$ mm for different crack radii, evaluated at points (a) A, (b) B, and (c) C.

under combined bending and contact load, especially for larger cracks. ‘Poor’ track support conditions increase this effect. Further, it is observed that the bending load has the highest influence in point A and the least impact in point C, which also has the shortest life.

Crack growth with passing traffic (in MGT) for the reference case under combined thermal and contact load is shown in Fig. 17b. Cold temperature generally reduces the rail life with a more pronounced effect observed for larger cracks and colder temperatures. The impact of a thermal load is most significant in point A and least significant in point C. Note that under thermal and contact load, each load cycle consists of one contact and one thermal cycle, which will overestimate the thermal effect. Further, the crack plane inclination is fixed. If the increased transverse deviation due to bending and/or thermal load for a propagating crack had been accounted for, the life reduction would likely have been more pronounced.

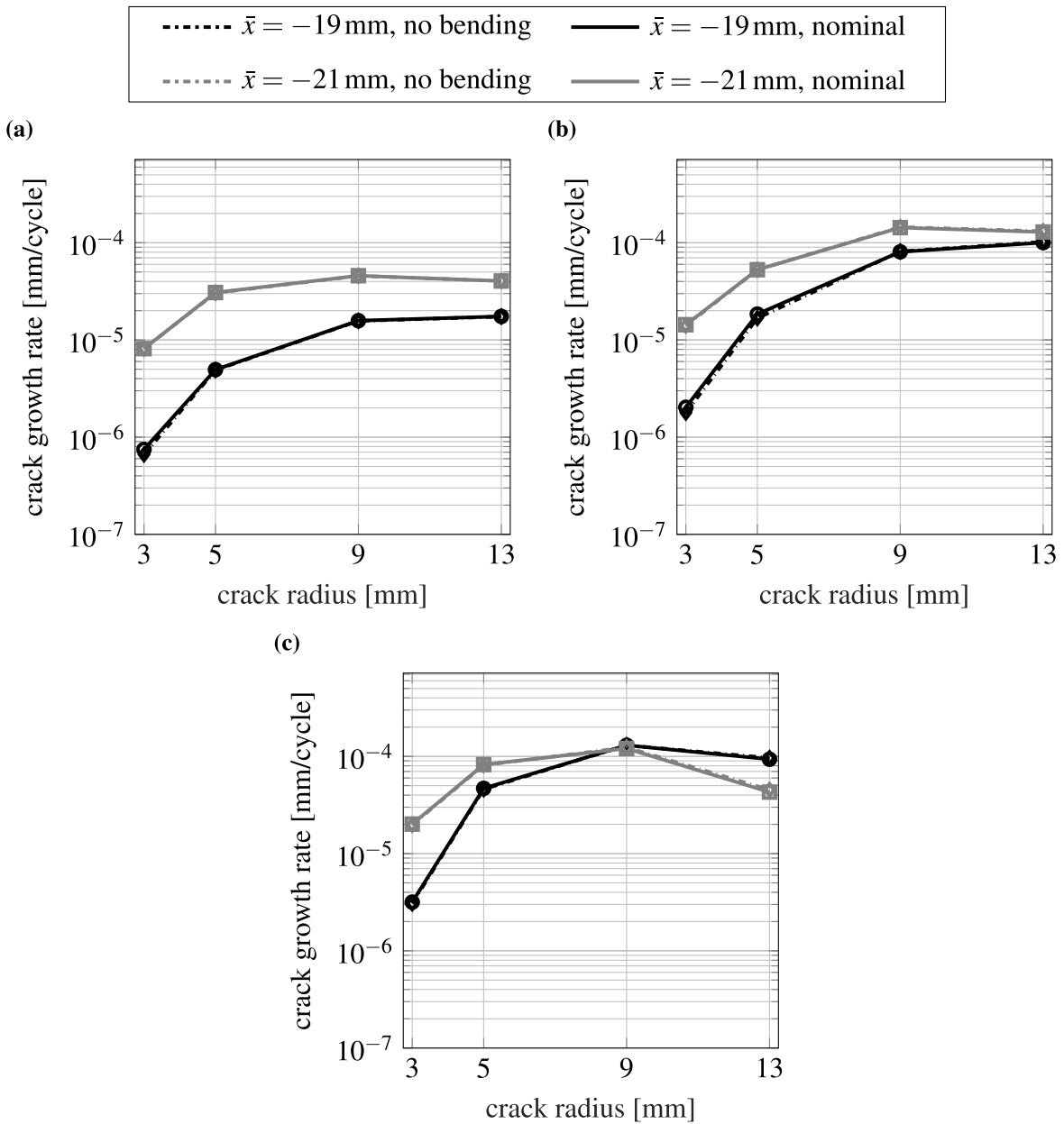


Fig. 12. Upper estimates of predicted crack growth rates under combined bending with 'nominal' track support conditions and a wheel load of $P = 7.5t$ with $f_{wr} = 0.3$ centred at $\bar{x} = -19$ mm and $\bar{x} = -21$ mm for different crack radii, evaluated at points (a) A, (b) B, and (c) C.

4. Concluding remarks

4.1. Observed crack growth trends

Head check crack growth directions and rates were numerically predicted to assess the influence of load conditions. Table 1 summarises the influence of studied operational parameters.

Regarding the influence of wheel load magnitude, contact load position, and tractive forces under pure contact loading, predicted results show that upward kinking is usually observed in the absence of a tractive force. Conditions in point C for pure contact load are similar to rolling contact conditions for wheels. Here cracks typically grow parallel to the surface or upwards to create surface pitting, see e.g., [45], which strengthens confidence in prediction results. Increasing the wheel load and moving the contact towards the gauge side increases predicted crack growth rates. This increase is more pronounced for smaller cracks, $r \leq 5$ mm. A tractive

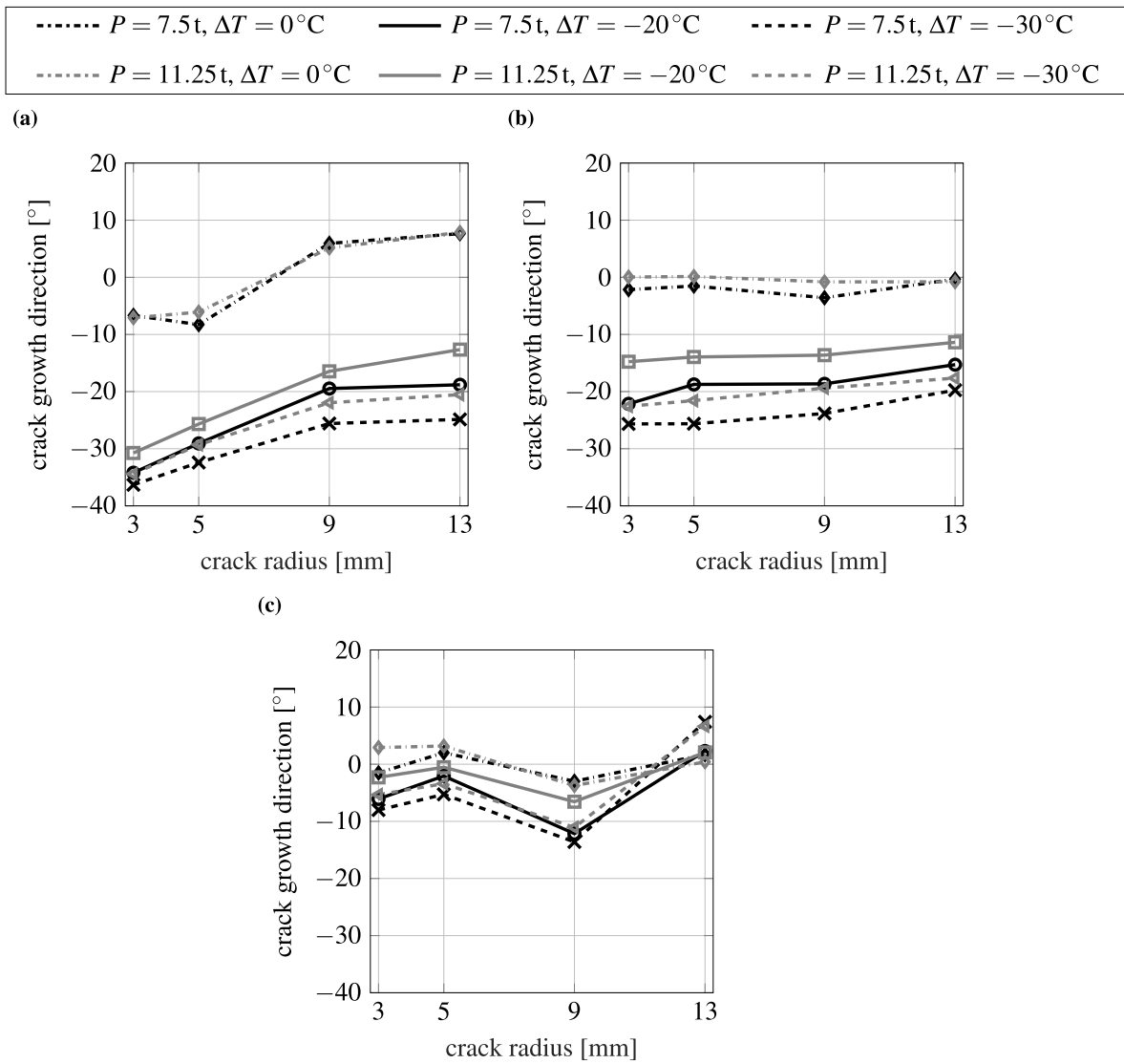


Fig. 13. Predicted crack growth directions under combined thermal and wheel load P with $f_{wr} = 0.3$ for different crack radii, evaluated at points (a) A, (b) B, and (c) C.

Table 1

Influence of the studied load variations with C: contact load, B: bending, and T: thermal.

load case	load parameters	crack propagation	
		direction	rate
C	wheel-rail traction	deeper	↑ for smaller cracks
	wheel load magnitude	shallower for higher C	↑ for higher C
	contact load position	shallower for $\bar{x} = -21$ mm	↑ for $\bar{x} = -21$ mm
B+C	compared to C with traction	deeper	↑
	'poor' track support conditions	deeper	↑
	wheel load magnitude	shallower for higher C	↑ for higher C
	contact load position	shallower for $\bar{x} = -21$ mm	↑ for $\bar{x} = -21$ mm
T+C	compared to C with traction	deeper	↑
	thermal load magnitude	deeper for higher T	↑ for higher T
	wheel load magnitude	shallower for higher C	↑ for higher C
	contact load position	shallower for $\bar{x} = -21$ mm	↑ for $\bar{x} = -21$ mm

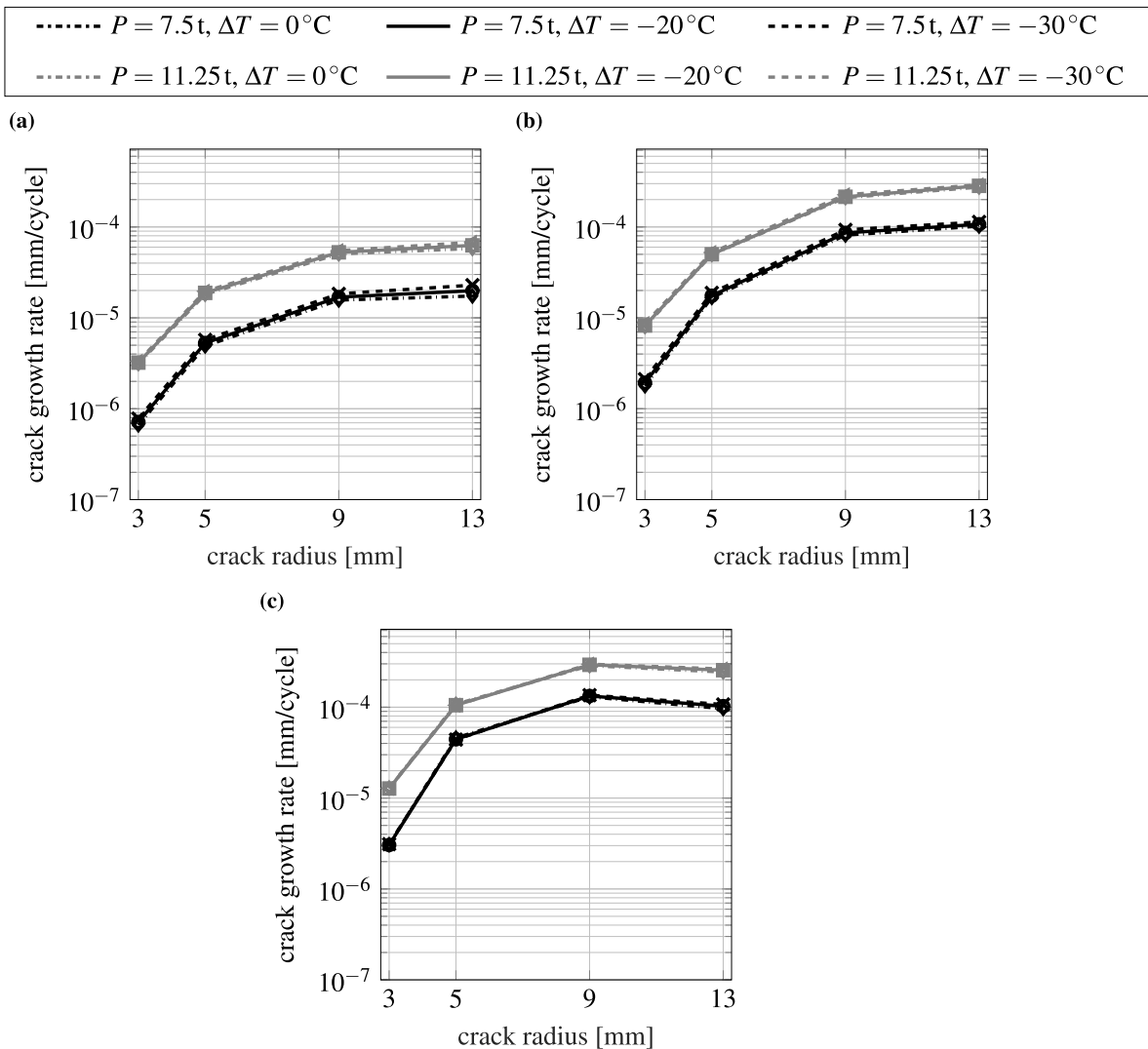


Fig. 14. Upper estimates of predicted crack growth rates under combined thermal and wheel load P with $f_{wr} = 0.3$ for different crack radii, evaluated at points (a) A, (b) B, and (c) C.

force introduces a propensity to grow downwards in point A, and increases crack growth rate for smaller cracks, $r \leq 5$ mm. Moving the contact load towards the gauge side gives shallower crack growth in the presence of traction.

For a combined bending and contact load, the crack tends to grow deeper into the rail than under a pure contact load. ‘Poor’ track support conditions slightly increase this effect. Predicted directions are not significantly affected by wheel load magnitudes. In general, the difference between pure contact and combined load predictions increases for larger crack sizes, especially for point A. This is in line with field observations that larger cracks grow mainly under the influence of bending [46]. Predicted rates under combined bending and contact are slightly higher than for the corresponding pure contact load case, with a higher influence under ‘poor’ track support conditions. Similar to the case of a pure contact load, growth rates increase when moving the contact load towards the gauge side, especially for point A. It also leads to shallower growth.

More downward growth is also observed in cases of contact load in combination with tensile forces due to decreasing temperature. This tendency is decreased in cases of increasing the contact load, or a contact load acting closer to the gauge side. Predicted crack growth rates under combined contact and thermal loads are very similar to (but slightly higher than) those of the corresponding pure contact load case.

Lastly, the rough estimation of crack growth as a function of transportation volumes (MGT) (presented in Fig. 17) can be contrasted to operational grinding intervals and occurring rail breaks.

Residual stresses in rails are neglected in the current study. The reason is that their magnitude will depend on the load history of the studied rail section. However, as residual stresses typically are compressive close to the rail surface, neglecting them would be a conservative assumption. In addition, material (pre)deformation and anisotropy may affect the growth direction and rate. In

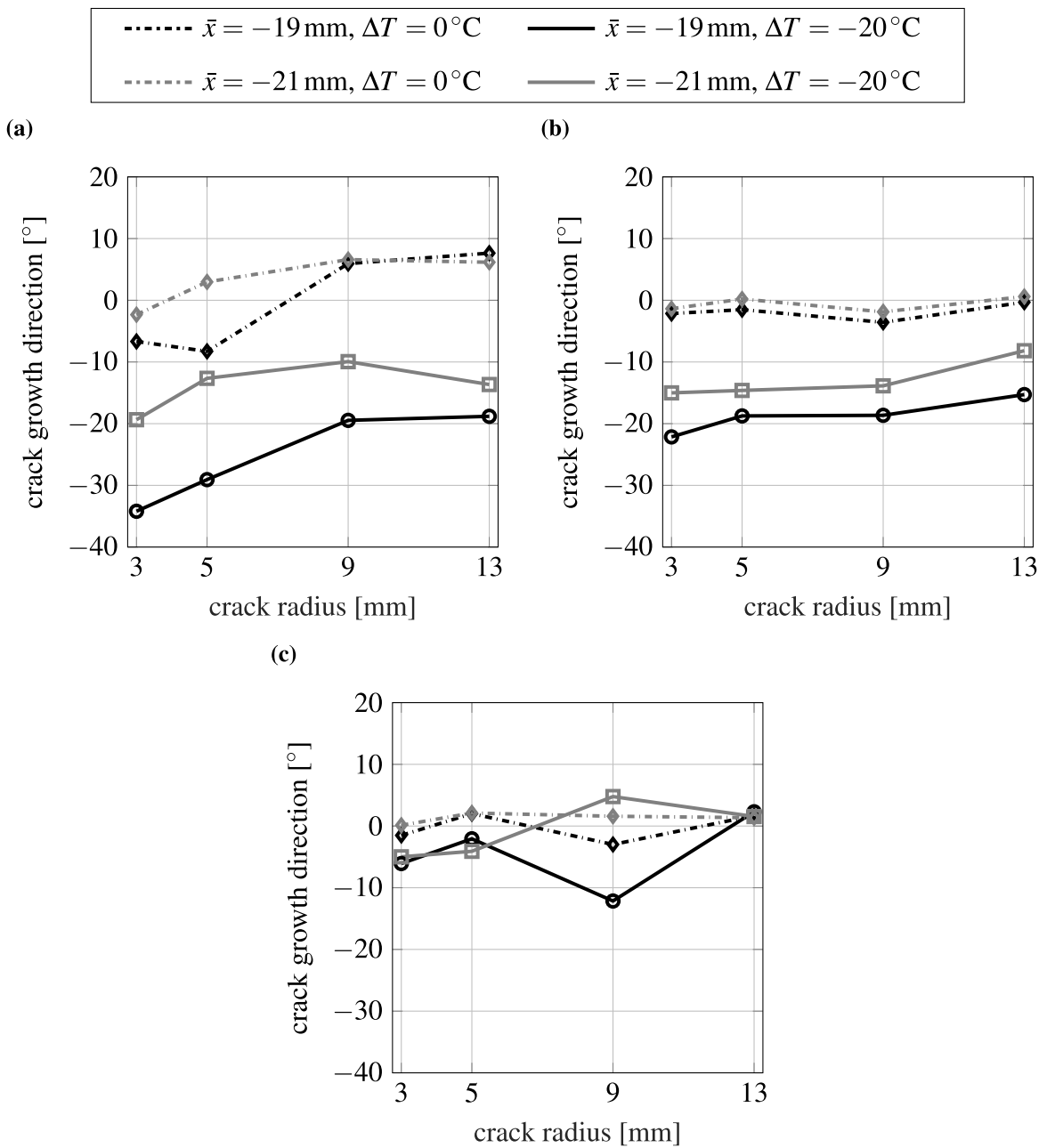


Fig. 15. Predicted crack growth directions under combined thermal and wheel load of $P = 7.5t$ with $f_{wr} = 0.3$ centred at $\bar{x} = -19\text{ mm}$ and $\bar{x} = -21\text{ mm}$ for different crack radii, evaluated at points (a) A, (b) B (b), and (c) C.

general, the crack propagation resistance increases by predeformation [47], which would counteract the effect of a residual stress. As of crack growth direction, the influence of predeformation seems limited, according to a recent study [47]. Given that, there are also several uncertainties, including the actual variation in contact load positions, and that much of the total life consists of forming the initial 3 mm crack, predicted lives are reasonably consistent with operational experiences.

4.2. Relation to squat and stud formation

A general trend seen in (almost) all investigated cases is that point A shows the greatest tendency to downward growth from the initial crack inclination and exhibits the slowest crack growth rate, whereas point C has the least tendency to downward growth. This means that point A wants to drag the crack plane down, but the crack plane propagates faster in points B and C. These predicted

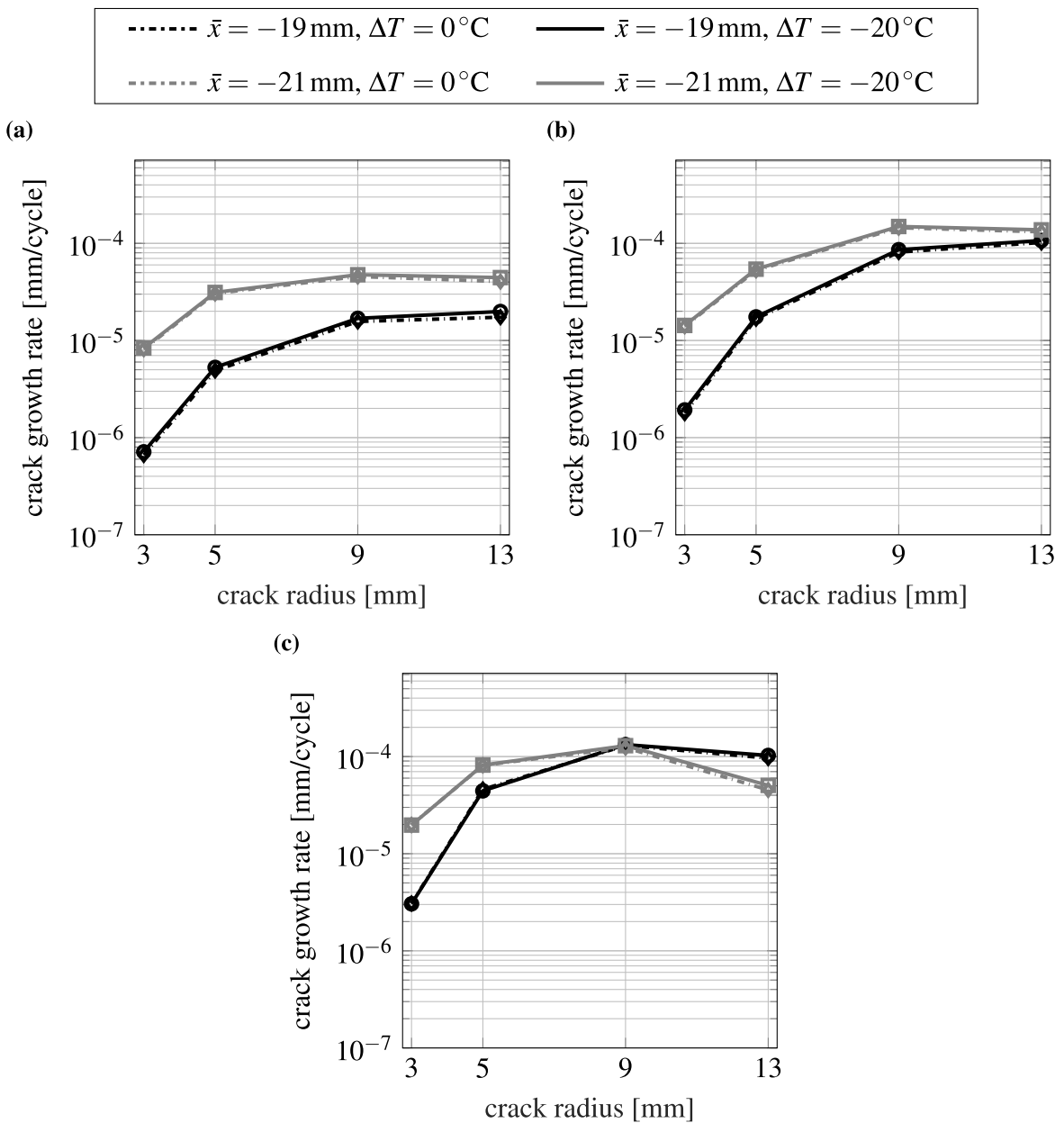


Fig. 16. Upper estimates of predicted crack growth rates under combined thermal and wheel load of $P = 7.5\text{t}$ with $f_{wr} = 0.3$ centred at $\bar{x} = -19\text{mm}$ and $\bar{x} = -21\text{mm}$ for different crack radii, evaluated at points (a) A, (b) B, and (c) C.

growth directions are in line with presented field observations of crack morphology of rail breaks in [46]. It is also consistent with the differing crack growth behaviour of studs and squats in field. As described in [18], studs are typically situated at the top surface of the rail head (and thereby corresponding mainly to point C). They usually grow shallowly into the rail. In contrast, squats may originate at, or extend to the edge of gauge corner cracks (and thereby also relate to point A) and tend to grow more downwards. Squats are therefore a higher safety risk than studs and need to be higher prioritised in maintenance planning. With reference to the current study, this could be interpreted that a squat-type defect with cracking extending towards the gauge corner could be prone to transverse growth, and should be given a high maintenance priority.

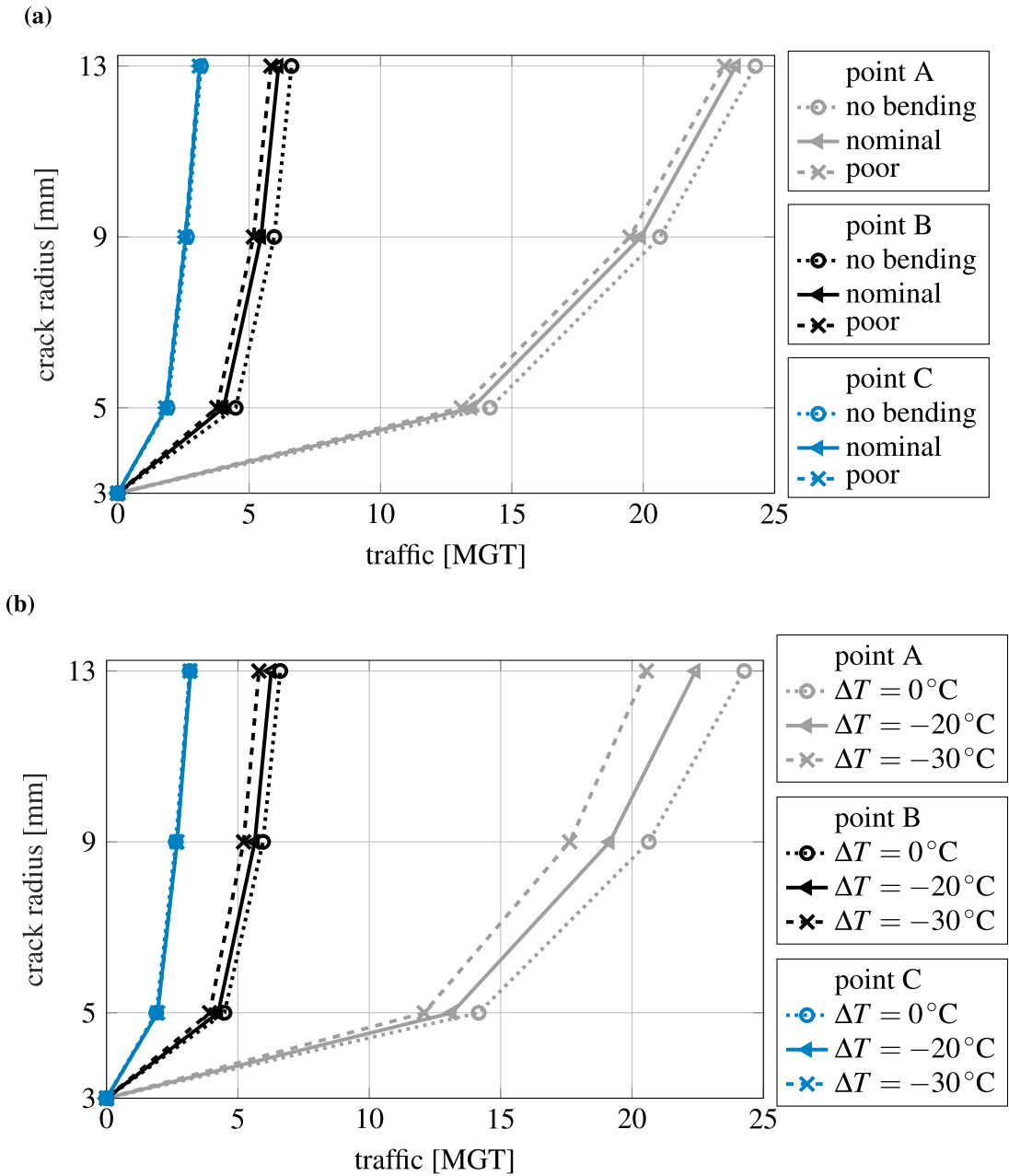


Fig. 17. Predicted fatigue lives from upper estimates of crack growth rates (in terms of passing axle loads in MGT) under (a) combined bending with different track support conditions and a wheel load; (b) combined thermal and a wheel load (wheel load $P = 7.5\text{ t}$ with $f_{wr} = 0.3$ in both cases).

4.3. Future work

The current study assumed an isolated stationary crack with frictionless crack faces. Considering a propagating crack and incorporating the effect of crack face friction, especially for longer cracks, would likely improve predictions and allow for better validation with field data. In addition, anisotropy existing close to the rail surface may impact crack growth predictions.

There are some additional factors to be considered for explicit modelling of a network of cracks usually seen in the field [35], such as spacing between cracks and length of each crack, which influences the predictions. Here, as an alternative, implicit crack modelling approaches, such as phase-field modelling [48], could be employed to take care of (some of) the aforementioned parameters. However, the developed crack growth criteria need to be reformulated in these methods.

CRediT authorship contribution statement

Mohammad Salahi Nezhad: Conceptualization, Methodology, Software, Validation, Writing – original draft, Writing – review & editing. **Elena Kabo:** Conceptualization, Methodology, Supervision, Resources, Writing – review & editing. **Anders Ekberg:** Conceptualization, Methodology, Supervision, Resources, Writing – review & editing. **Fredrik Larsson:** Conceptualization, Methodology, Supervision, Resources, Writing – review & editing.

Source of funding

The work has been financed by CHARMEC – Centre of Excellence in Railway MEchanics at CHAlmers University of Technology and the Horizon Europe research and innovation programme in Europe Rail project IAM4RAIL under grant agreement No. 101101966.

Declaration of competing interest

The authors declare that they have no known competing financial interests or personal relationships that could have appeared to influence the work reported in this paper.

Acknowledgements

The work is part of activities within the Competence Centre CHARMEC (www.chalmers.se/charmec). They are funded within the Horizon Europe research and innovation programme in Europe Rail project IAM4RAIL under grant agreement No. 101101966. The computations were performed on resources provided by Chalmers e-Commons (C3SE). The authors would like to thank Professor Jens Nielsen at Chalmers University of Technology for kindly providing analyses of bending moments for the study.

Data availability

Data will be made available on request.

References

- [1] Johnson KL. The strength of surfaces in rolling contact. Proceedings of the institution of mechanical engineers. Part C: Mech Eng Sci 1989;203(3):151–63. http://dx.doi.org/10.1243/PIME_PROC_1989_203_100_02.
- [2] Magel EE. Rolling contact fatigue: a comprehensive review. US department of transportation, federal railroad administration; 2011, p. 132. <http://dx.doi.org/10.4224/23000318>.
- [3] Cannon DF, Edell K-O, Grassie SL, Sawley K. Rail defects: an overview. Fatigue Fract Eng Mater Struct 2003;26(10):865–86. <http://dx.doi.org/10.1046/j.1460-2695.2003.00693.x>.
- [4] Bogdański S, Olzak M, Stupnicki J. Numerical modelling of a 3D rail RCF 'squat'-type crack under operating load. Fatigue Fract Eng Mater Struct 1998;21(8):923–35. <http://dx.doi.org/10.1046/j.1460-2695.1998.00082.x>.
- [5] Mai SH, Gravouil A, Nguyen-Tajan ML, Trollé B. Numerical simulation of rolling contact fatigue crack growth in rails with the rail bending and the frictional contact. Eng Fract Mech 2017;174:196–206. <http://dx.doi.org/10.1016/j.engfracmech.2016.12.019>.
- [6] Afridi AH, Zhu H, Camacho ET, Deng G, Li H. Numerical modeling of rolling contact fatigue cracks in the railhead. Eng Fail Anal 2023;143:106838. <http://dx.doi.org/10.1016/j.engfailanal.2022.106838>.
- [7] Rodriguez-Arana B, Bergara A, Gil-Negrete N, Nieto J. XFEM rolling contact fatigue crack propagation in railways considering creepages on contact shear stresses. Eng Fract Mech 2022;276:108896. <http://dx.doi.org/10.1016/j.engfracmech.2022.108896>.
- [8] Bogdański S, Stupnicki J, Brown MW, Cannon DF. A two dimensional analysis of mixed-mode rolling contact fatigue crack growth in rails. Eur Struct Integr Soc 1999;25:235–48. [http://dx.doi.org/10.1016/S1566-1369\(99\)80018-1](http://dx.doi.org/10.1016/S1566-1369(99)80018-1).
- [9] Bogdański S, Brown MW. Modelling the three-dimensional behaviour of shallow rolling contact fatigue cracks in rails. Wear 2002;253(1):17–25. [http://dx.doi.org/10.1016/S0043-1648\(02\)00078-9](http://dx.doi.org/10.1016/S0043-1648(02)00078-9).
- [10] Fletcher DI, Corteen J, Wilby A. Rough surface rolling contact fatigue crack stress intensity factor calculation for modern rail steels. Wear 2024;540–541:205231. <http://dx.doi.org/10.1016/j.wear.2023.205231>.
- [11] Floros D, Ekberg A, Larsson F. Evaluation of crack growth direction criteria on mixed-mode fatigue crack growth experiments. Int J Fatigue 2019;129:105075. <http://dx.doi.org/10.1016/j.ijfatigue.2019.04.013>.
- [12] Floros D, Ekberg A, Larsson F. Evaluation of mixed-mode crack growth direction criteria under rolling contact conditions. Wear 2020;448–449:203184. <http://dx.doi.org/10.1016/j.wear.2020.203184>.
- [13] Trollé B, Baietto M-C, Gravouil A, Mai SH, Prabel B. 2D fatigue crack propagation in rails taking into account actual plastic stresses. Eng Fract Mech 2014;123:163–81. <http://dx.doi.org/10.1016/j.engfracmech.2014.03.020>.
- [14] Salahi Nezhad M, Floros D, Larsson F, Kabo E, Ekberg A. Numerical predictions of crack growth direction in a railhead under contact, bending and thermal loads. Eng Fract Mech 2022;261:108218. <http://dx.doi.org/10.1016/j.engfracmech.2021.108218>.
- [15] Salahi Nezhad M, Larsson F, Kabo E, Ekberg A. Numerical prediction of railhead rolling contact fatigue crack growth. Wear 2023;530–531:205003. <http://dx.doi.org/10.1016/j.wear.2023.205003>.
- [16] Hengeveld ST, Leonetti D, Snijder B, Maljaars J. Prediction of fatigue crack paths including crack-face friction for an inclined edge crack subjected to mixed mode loading. Procedia Struct Integr 2024;54:34–43. <http://dx.doi.org/10.1016/j.prostr.2024.01.053>.
- [17] Salahi Nezhad M, Larsson F, Kabo E, Ekberg A. Finite element analyses of rail head cracks: Predicting direction and rate of rolling contact fatigue crack growth. Eng Fract Mech 2024;310:110503. <http://dx.doi.org/10.1016/j.engfracmech.2024.110503>.
- [18] Grassie SL. Studs and squats: The evolving story. Wear 2016;366–367:194–9. <http://dx.doi.org/10.1016/j.wear.2016.03.021>.

- [19] Andersson R, Larsson F, Kabo E. Evaluation of stress intensity factors under multiaxial and compressive conditions using low order displacement or stress field fitting. *Eng Fract Mech* 2018;189:204–20. <http://dx.doi.org/10.1016/j.engfracmech.2017.11.015>.
- [20] Wu Y, Chung LP, Huang P, Welsby D, Mutton P, et al. Effect of creepages on stress intensity factors of rolling contact fatigue cracks. *Eng Fract Mech* 2023;289:109477. <http://dx.doi.org/10.1016/j.engfracmech.2023.109477>.
- [21] Sun CT, Jin Z-H. *Fracture mechanics*. Academic Press; 2012, p. 311. <http://dx.doi.org/10.1016/C2009-0-63512-1>.
- [22] Paris P, Erdogan F. A critical analysis of crack propagation laws. *J Basic Eng* 1963;85(4):528–33. <http://dx.doi.org/10.1115/1.3656900>.
- [23] Wong SL, Bold PE, Brown MW, Allen RJ. Fatigue crack growth rates under sequential mixed-mode I and II loading cycles. *Fatigue Fract Eng Mater Struct* 2000;23(8):667–74. <http://dx.doi.org/10.1046/j.1460-2695.2000.00342.x>.
- [24] Skyttebol A, Josefson BL, Ringsberg JW. Fatigue crack growth in a welded rail under the influence of residual stresses. *Eng Fract Mech* 2005;72:271–85. <http://dx.doi.org/10.1016/j.engfracmech.2004.04.009>.
- [25] Socie D, Marquis G. *Multiaxial fatigue*. SAE International; 2000, p. 484.
- [26] CEN. *Railway applications - track - rail - part 1: vignole railway rails 46 kg/m and above*. EN 13674-1:2011. European Committee for Standardization; 2011.
- [27] *ABAQUS analysis user's manual (version 2020)*. Dassault Systèmes Simulia Corp.; 2020.
- [28] Dollevoet RPBJ. Design of an anti head check profile based on stress relief (Ph.D. thesis), University of Twente; 2010, p. 151. <http://dx.doi.org/10.3990/1.9789036530736>.
- [29] Stock R, Pippan R. RCF and wear in theory and practice—The influence of rail grade on wear and RCF. *Wear* 2011;271(1–2):125–33. <http://dx.doi.org/10.1016/j.wear.2010.10.015>.
- [30] Heyder R, Girsch G. Testing of HSH® rails in high-speed tracks to minimise rail damage. *Wear* 2005;258(7–8):1014–21. <http://dx.doi.org/10.1016/j.wear.2004.03.050>.
- [31] *ABAQUS/CAE user's manual (version 2020)*. Dassault Systèmes Simulia Corp.; 2020.
- [32] Belytschko T, Black T. Elastic crack growth in finite elements with minimal remeshing. *Internat J Numer Methods Engrg* 1999;45:601–20. [http://dx.doi.org/10.1002/\(SICI\)1097-0207\(19990620\)45:5<601::AID-NME598>3.0.CO;2-S](http://dx.doi.org/10.1002/(SICI)1097-0207(19990620)45:5<601::AID-NME598>3.0.CO;2-S).
- [33] Moës N, Dolbow J, Belytschko T. A finite element method for crack growth without remeshing. *Internat J Numer Methods Engrg* 1999;46:131–50. [http://dx.doi.org/10.1002/\(SICI\)1097-0207\(19990910\)46:1<131::AID-NME726>3.0.CO;2-J](http://dx.doi.org/10.1002/(SICI)1097-0207(19990910)46:1<131::AID-NME726>3.0.CO;2-J).
- [34] Fletcher DI, Hyde P, Kapoor A. Modelling and full-scale trials to investigate fluid pressurisation of rolling contact fatigue cracks. *Wear* 2008;265(9):1317–24. <http://dx.doi.org/10.1016/j.wear.2008.02.025>.
- [35] Meyer KA, Gren D, Ahlström J, Ekberg A. A method for in-field railhead crack detection using digital image correlation. *Int J Rail Transp* 2022;10(6):675–94. <http://dx.doi.org/10.1080/23248378.2021.2021455>.
- [36] Johnson KL. *Contact mechanics*. Cambridge University Press; 1985, p. 452. <http://dx.doi.org/10.1017/CBO9781139171731>.
- [37] Timoshenko SP, Goodier JN. *Theory of elasticity*. McGraw-Hill; 1951, p. 506.
- [38] IRS 70712: Rail defects. International Union of Railways (UIC), 1st ed., 2018-5; 2018, p. 115.
- [39] Roolevelt T. Measurement of wheel-rail contact forces. In: *Symposium of advances in contact mechanics: a tribute to prof. J.J.Kalker*. The Netherlands: TU Delft; 2008.
- [40] Skrypnik R, Nielsen JCO, Ekh M, Pålsson BA. Metamodelling of wheel-rail normal contact in railway crossings with elasto-plastic material behaviour. *Eng Comput* 2019;35:139–55. <http://dx.doi.org/10.1007/s00366-018-0589-3>.
- [41] Ekberg A, Åkesson B, Kabo E. Wheel/rail rolling contact fatigue – probe, predict, prevent. *Wear* 2014;314(1–2):2–12. <http://dx.doi.org/10.1016/j.wear.2013.12.004>.
- [42] Cvetkovski K, Ahlström J, Norell M, Persson C. Analysis of wear debris in rolling contact fatigue cracks of pearlitic railway wheels. *Wear* 2014;314(1):51–6. <http://dx.doi.org/10.1016/j.wear.2013.11.049>.
- [43] Nielsen JCO, Igeland A. Vertical dynamic interaction between train and track influence of wheel and track imperfections. *J Sound Vib* 1995;187(5):825–39. <http://dx.doi.org/10.1006/jsvi.1995.0566>.
- [44] *MATLAB 9.7.0.1190202 (version R2019b)*. The MathWorks Inc.; 2019.
- [45] Ekberg A, Kabo E. Fatigue of railway wheels and rails under rolling contact and thermal loading—an overview. *Wear* 2005;258(7):1288–300. <http://dx.doi.org/10.1016/j.wear.2004.03.039>.
- [46] Ekberg A, Kabo E. Surface fatigue initiated transverse defects and broken rails – an international review. 2014, p. 24. <https://research.chalmers.se/en/publication/?id=203928>.
- [47] Gren D, Ahlström J. Fatigue crack propagation on uniaxial loading of biaxially predeformed pearlitic rail steel. *Metals* 2023;13(10):1726. <http://dx.doi.org/10.3390/met13101726>.
- [48] Polančec T, Lesičar T, Tonković Z, Glodež S. Modelling of rolling-contact fatigue pitting phenomena by phase field method. *Wear* 2023;532–533:205068. <http://dx.doi.org/10.1016/j.wear.2023.205068>.